

BubR1 recruitment to the kinetochore via Bub1 enhances spindle assembly checkpoint signaling

Anand Banerjee^{a,†,*}, Chu Chen^{b,†}, Lauren Humphrey^b, John J. Tyson^c, and Ajit P. Joglekar^{b,*}

^aAcademy of Integrated Science and ^cDepartment of Biological Sciences, Virginia Polytechnic Institute & State University, Blacksburg, VA 24601; ^bCell & Developmental Biology, University of Michigan Medical School, Ann Arbor, MI 48109

ABSTRACT During mitosis, unattached kinetochores in a dividing cell activate the spindle assembly checkpoint (SAC) and delay anaphase onset by generating the anaphase-inhibitory mitotic checkpoint complex (MCC). These kinetochores generate the MCC by recruiting its constituent proteins, including BubR1. In principle, BubR1 recruitment to signaling kinetochores should increase its local concentration and promote MCC formation. However, in human cells BubR1 is mainly thought to sensitize the SAC to silencing. Whether BubR1 localization to signaling kinetochores by itself enhances SAC signaling remains unknown. Therefore, we used ectopic SAC activation (eSAC) systems to isolate two molecules that recruit BubR1 to the kinetochore, the checkpoint protein Bub1 and the KI and MELT motifs in the kinetochore protein KNL1, and observed their contribution to eSAC signaling. Our quantitative analyses and mathematical modeling show that Bub1-mediated BubR1 recruitment to the human kinetochore promotes SAC signaling and highlight BubR1's dual role of strengthening the SAC directly and silencing it indirectly.

Monitoring Editor

Kerry Bloom
University of North Carolina,
Chapel Hill

Received: Mar 09, 2022

Revised: Jun 15, 2022

Accepted: Jun 21, 2022

INTRODUCTION

The spindle assembly checkpoint (SAC) is a cell cycle control that minimizes chromosome missegregation during cell division (Musacchio, 2015; Lara-Gonzalez *et al.*, 2021b). It is activated by kinetochores that are not stably attached to the plus ends of spindle microtubules. These kinetochores generate a diffusible anaphase-inhibitory signal known as the mitotic checkpoint complex (MCC). The MCC delays anaphase onset to avert cell division in the presence of unattached kinetochores.

This article was published online ahead of print in MBoC in Press (<http://www.molbiolcell.org/cgi/doi/10.1091/mbc.E22-03-0085>) on June 29, 2022.

[†]These authors contributed equally.

Conflict of interest: The authors declare that no competing financial interests exist.

*Address correspondence to: Ajit P. Joglekar (ajitj@umich.edu); Anand Banerjee (anandban@vt.edu).

Abbreviations used: eSAC, ectopic spindle assembly checkpoint activation; MCC, mitotic checkpoint complex; SAC, spindle assembly checkpoint.

© 2022 Banerjee, Chen, *et al.* This article is distributed by The American Society for Cell Biology under license from the author(s). Two months after publication it is available to the public under an Attribution–Noncommercial–Share Alike 4.0 International Creative Commons License (<http://creativecommons.org/licenses/by-nc-sa/4.0>).

"ASCB®," "The American Society for Cell Biology®," and "Molecular Biology of the Cell®" are registered trademarks of The American Society for Cell Biology.

The rate at which an unattached kinetochore generates the MCC depends on its ability to recruit SAC signaling proteins, which include constituent proteins of the MCC: Bub1-Bub3, BubR1-Bub3, Mad1-Mad2, and Cdc20 (Figure 1A, dashed square). This signaling cascade generates either the MCC itself, its subcomplex C-Mad2-Cdc20, or both. Given this knowledge, it is reasonable to expect that the rate of MCC generation at a kinetochore will increase with higher recruitment of the MCC components to the kinetochore (Collin *et al.*, 2013; Lara-Gonzalez *et al.*, 2021a; Piano *et al.*, 2021). Interestingly, however, this expectation appears to not hold true for BubR1. Disruption of BubR1 recruitment to unattached kinetochores does not reduce the duration of SAC-induced mitotic arrest in nocodazole-treated cells (Overlack *et al.*, 2015; Zhang *et al.*, 2015). This is because BubR1 recruits to the kinetochore protein phosphatase 2A (PP2A), which promotes SAC silencing (Foley *et al.*, 2011; Nijenhuis *et al.*, 2014; Qian *et al.*, 2017). Despite this knowledge, it is crucial to determine whether BubR1 recruitment to the kinetochore also promotes SAC signaling by enhancing MCC assembly. This BubR1 activity can be crucial for minimizing chromosome missegregation during normal cell division wherein a small number of unattached kinetochores must activate the SAC and delay anaphase onset (Roy *et al.*, 2020).

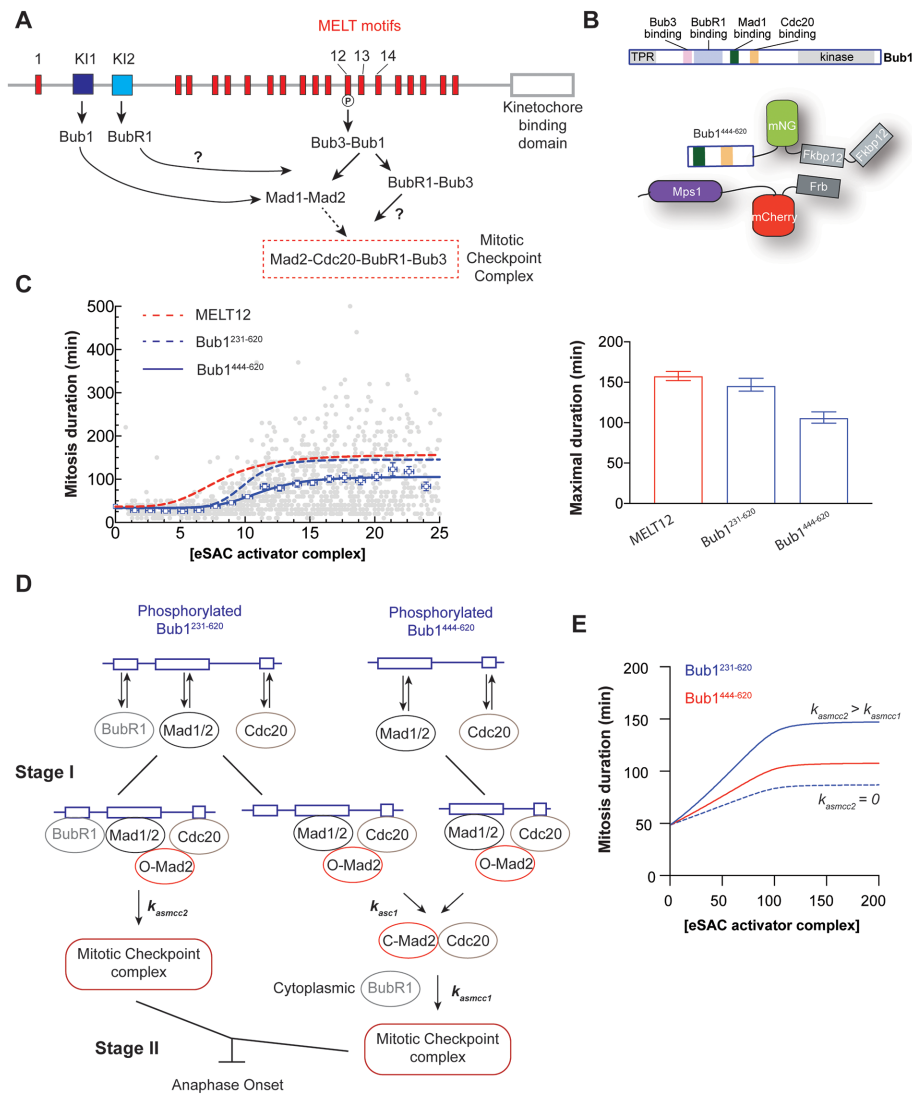


FIGURE 1: The contribution of Bub1-BubR1 heterodimerization to MCC assembly in eSAC signaling. (A) Schematic at the top displays the domain organization of human Knl1. Below is a simplified schematic displaying the pathways that recruit SAC signaling proteins to unattached kinetochores. (B) Schematic at the top displays the domain organization of human Bub1. The cartoon represents the eSAC system. (C) Dose-response data for an eSAC system that uses Bub1⁴⁴⁴⁻⁶²⁰ as the phosphodomains. Each gray circle represents a single cell ($n = 1920$ from two technical replicates; 139 and 155 are the lower and upper 95% confidence intervals). The blue squares represent the mean values of the dose-response data binned according to mCherry fluorescence. Vertical and horizontal lines represent SEM. The solid blue curve displays the least squares four-parameter sigmoidal fitted to the binned mean values. Hill equation fits for dose-response data for one MELT motif (MELT12, dashed red curve) and an extended Bub1²³¹⁻⁶²⁰ phosphodomain containing the Bub3- and BubR1-binding sites (dashed blue curve) from our previous study have been superimposed for comparison (Chen *et al.*, 2019). Note that these and the Bub1⁴⁴⁴⁻⁶²⁰ phosphodomain data were obtained using identical imaging conditions to enable their direct comparison. The bar graph on the right displays the maximal mitotic duration estimated by the fit. Error bars represent 95% confidence intervals of the fitted maximal mitotic duration. (D) Cartoon displays the simplified scheme used to simulate the generation of MCC by the eSAC system. (E) Numerical simulation of the dose-response curves by assuming the assembly of signaling complexes and ultimately the MCC as shown in D followed by a model described by He *et al.* (2011).

In this study, we examine the contribution of BubR1 recruitment to kinetochore-mediated SAC signaling. Using the ectopic SAC activation (eSAC) system, we find that the binding of BubR1 to Bub1 elevates Bub1-mediated MCC generation (Chen *et al.*, 2019). On

the other hand, the recruitment of Bub1 and BubR1 via the “KI” motifs in the kinetochore protein Knl1 does not contribute to MCC generation mediated by the “MELT” motifs within the Knl1 phosphodomain (Bolanos-Garcia *et al.*, 2011; Kiyomitsu *et al.*, 2011; Primorac *et al.*, 2013; Vleugel *et al.*, 2013; Krenn *et al.*, 2014; Zhang *et al.*, 2014). We also establish a mathematical model to elucidate the mechanistic details of the SAC signaling cascade that generates the MCC. Finally, we also demonstrate that BubR1 recruitment to the kinetochore via Bub1 promotes SAC signaling.

RESULTS AND DISCUSSION

The BubR1-binding domain of Bub1 promotes Bub1-mediated MCC assembly

Bub1 coordinates the rate-limiting step in MCC assembly: the formation of the closed-Mad2-Cdc20 (Mad2:Cdc20) subcomplex (Faesen *et al.*, 2017; Lara-Gonzalez *et al.*, 2021a; Piano *et al.*, 2021). Mad2:Cdc20 must bind BubR1 to complete MCC formation. BubR1 is recruited to the kinetochore by Bub1, and the KI motifs and MELT motifs in KNL1 (Bolanos-Garcia *et al.*, 2011; Kiyomitsu *et al.*, 2011; Overlack *et al.*, 2015; Zhang *et al.*, 2016). Whether this BubR1 recruitment promotes MCC formation remains unclear. In fission yeast, BubR1 binding to Bub1 is essential for SAC activity (Leontiou *et al.*, 2019). However, BubR1 is unlikely to be recruited to budding yeast kinetochores (Tromer *et al.*, 2016; Roy *et al.*, 2022), and in nocodazole-treated HeLa cells, the disruption of Bub1-mediated BubR1 recruitment slightly strengthens the SAC (Overlack *et al.*, 2015; Zhang *et al.*, 2016). The latter phenotype arises because the disruption of BubR1 recruitment also disrupts BubR1-mediated PP2A recruitment to the kinetochore (Elowe *et al.*, 2007; Suijkerbuijk *et al.*, 2012). Therefore, to isolate and quantitatively define the effect of Bub1-BubR1 heterodimerization on Bub1-mediated MCC assembly, we used the eSAC system.

Forced dimerization of a fragment of the central domain of Bub1 with Mps1 delays anaphase onset in HeLa cells, budding yeast, and fission yeast (Aravamudhan *et al.*, 2015; Yuan *et al.*, 2017; Chen *et al.*, 2019; Leontiou *et al.*, 2019). In HeLa cells, induced dimerization of the central domain of Bub1 (Bub1²³¹⁻⁶²⁰-mNG-2xFkbp12; diagram in Figure 1B) with the Mps1 kinase domain (Frb-mCherry-Mps1⁵⁰⁰⁻⁸¹⁷) produces a dosage-dependent increase in the duration of mitosis with a maximal duration of ~145 min (Figure 1C, replotted for comparison from Chen *et al.*, 2019). Importantly, the extended mitosis was due to increased Mad2-Cdc20 and

MCC formation in HeLa cells and fission yeast (Leontiou *et al.*, 2019; Roy *et al.*, 2022). To assess the contribution of Bub1-BubR1 heterodimerization to Bub1-mediated MCC assembly, we created a truncated Bub1 phosphodomain lacking the BubR1 heterodimerization domain (Bub1⁴⁴⁴⁻⁶²⁰-mNG-2xFkbp12) (Overlack *et al.*, 2015; Zhang *et al.*, 2016). Rapamycin-induced dimerization of this phosphodomain with Frb-mCherry-Mps1⁵⁰⁰⁻⁸¹⁷ elicited a significantly weaker eSAC activity, with a maximal mitotic duration of 105 ± 6 min (Figure 1C, estimated from a fit with the four-parameter Hill equation; the range indicates 95% confidence intervals; see *Materials and Methods* for details). We previously found that deletion of the Bub3-binding GLEBS domain from the Bub1 phosphodomain does not decrease its eSAC activity (Roy *et al.*, 2022). Therefore, Bub1-BubR1 heterodimerization promotes MCC formation mediated by the Bub1 phosphodomain. It should be noted that we cannot rule out the possibility that the large truncation used here affects Mad1 interaction with the eSAC to some extent.

Simulation of the signaling activity of the Bub1 phosphodomains

To quantitatively understand the dose-response dependence of the eSAC system, we constructed a mathematical model by considering the events at the Bub1 phosphodomain before MCC assembly. This model consists of two stages. In the first stage, we calculate the steady-state concentrations of signaling complexes assembled by the Bub1 eSAC phosphodomains assuming mass action kinetics (Figure 1D; Eqs. 1–4 and 5a–5j). Bub1²³¹⁻⁶²⁰ recruits BubR1 and Cdc20 independently of its phosphorylation state or the presence of other bound proteins; Bub1⁴⁴⁴⁻⁶²⁰ recruits only Cdc20 (Di Fiore *et al.*, 2015; Overlack *et al.*, 2015). Both phosphodomains are activated by Mps1-mediated phosphorylation, after which they recruit Mad1-Mad2 (abbreviated as Mad1/2) (London and Biggins, 2014; Faesen *et al.*, 2017; Ji *et al.*, 2017; Zhang *et al.*, 2017). Therefore, the signaling activity of each phosphodomain will be proportional to the amount of Frb-mCherry-Mps1⁵⁰⁰⁻⁸¹⁷, that is, the eSAC dosage in the cell, and it will be limited by the cellular Mad1/2 abundance when the eSAC dosage exceeds Mad1/2 abundance (shown later; see Supplemental Figure S1A). Through these interactions, Bub1²³¹⁻⁶²⁰ can assemble two types of signaling complexes: one that contains Cdc20, BubR1, and Mad1/2 and one containing only Cdc20 and Mad1/2; Bub1⁴⁴⁴⁻⁶²⁰ forms only the signaling complex containing Mad1/2 and Cdc20 (Figure 1D, left).

We simulated MCC formation by the Bub1:BubR1:Mad1/2:Cdc20 signaling complex as follows. Because Mad2-Cdc20 formation is the rate-limiting step in MCC assembly (Faesen *et al.*, 2017), the Bub1²³¹⁻⁶²⁰:BubR1:Mad1/2:Cdc20 signaling complex first assembles Mad2:Cdc20 with the rate constant k_{asc1} . The newly formed Mad2:Cdc20 can bind BubR1 either within the signaling complex with the rate constant k_{asmcc2} or in the cytosol with the rate constant k_{asmcc1} (Figure 1D, bottom). The model assumes that all the Mad2:Cdc20 formed by Bub1²³¹⁻⁶²⁰:BubR1:Mad1/2:Cdc20 binds BubR1 within the signaling complex. However, allowing a reasonable fraction of Mad2:Cdc20 to escape from the signaling complex does not affect the overall behavior of the model (unpublished data). Because Mad2:Cdc20 formation is the rate-limiting step, we reduce the number of free parameters by assuming that k_{asc1} and k_{asmcc2} are equal. The cumulative MCC formed by Bub1²³¹⁻⁶²⁰ is the sum of MCC formed from these two processes. All Mad2-Cdc20 generated by Bub1⁴⁴¹⁻⁶²⁰:Mad1/2:Cdc20 form MCC in the cytosol. In the second stage of the model (Figure 1D; Eqs. 5k–5n; *Materials and Methods*), the MCC formed by both processes modulates cyclin B degradation and thereby controls the timing of metaphase-to-

anaphase transition (Supplemental Figure S1B) (He *et al.*, 2011; Chen *et al.*, 2019).

We first simulated the dose-response curve for the Bub1⁴⁴⁴⁻⁶²⁰ eSAC involving only cytoplasmic MCC assembly. We retained protein concentrations used in the original model of He *et al.* (2011) and used reasonable rate constants for Mad2:Cdc20 formation (k_{asc1}) and cytosolic MCC formation (k_{asmcc1} ; Figure 1E, red curve; see Supplemental Table S1 for protein concentrations and rate constants used). Next, we considered MCC formation by the Bub1²³¹⁻⁶²⁰ eSAC, which can assemble the MCC within the signaling complex or the cytosol. If BubR1 recruited by the signaling complex does not participate in MCC formation (i.e., $k_{asmcc2} = 0$), the simulation produced a dose-response curve with a lower maximal response (dotted blue line in Figure 1E). This is because BubR1 bound to Bub1 cannot participate in any form of MCC assembly. Therefore, the only effect of Bub1-BubR1 heterodimerization is a reduced cytosolic BubR1 concentration and, consequently, a correspondingly reduced rate of MCC generation. This model prediction is inconsistent with the data. Therefore, BubR1 recruited by Bub1 must promote MCC formation within the eSAC-signaling complex. Following this insight, we assumed that k_{asmcc2} is 10-fold higher than k_{asmcc1} for cytosolic MCC assembly. With this change, the simulation produced a longer delay in anaphase onset, matching our observations.

This simulation provides two insights. First, it supports the observation that Bub1-BubR1 heterodimerization promotes MCC formation by the eSAC based on the Bub1 phosphodomain. It also indicates that if Bub1-BubR1 heterodimerization does not promote MCC formation, it will lead to BubR1 sequestration and a reduced rate of cytosolic MCC formation. This effect plays a critical role in the experiments that follow.

KI motifs suppress the signaling strength of the eSAC phosphodomain

The KI motifs, so named because they contain lysine and isoleucine residues critical for their activities, recruit Bub1 and BubR1 to the human kinetochore (Figure 1A). The first KI motif (KI1) is thought to exclusively bind Bub1, whereas the second motif (KI2) binds BubR1 (Bolanos-Garcia *et al.*, 2011; Kiyomitsu *et al.*, 2011; Krenn *et al.*, 2014, 2012). A prior study concluded that the KI motifs cooperate with the first MELT motif in KNL1 to strengthen SAC signaling (Vleugel *et al.*, 2013; Krenn *et al.*, 2014). However, it is unclear whether the activity of regulatory enzymes (eg., PLK1, PP2A) bound to Bub1 and BubR1 plays a role in these observations (Nijenhuis *et al.*, 2014; von Schubert *et al.*, 2015; Jia *et al.*, 2016). Therefore, to test whether the KI motifs directly promote MCC assembly and delineate their roles, we developed an eSAC phosphodomain comprising the two KI motifs and a MELT motif (Knl1¹⁶⁰⁻²⁵⁶) (Figure 2A). We also created a variant phosphodomain with inactive KI motifs (Krenn *et al.*, 2012). If Bub1 and BubR1 recruitment via the KI motifs enhances MELT motif activity, this will be apparent as increased signaling strength of this new eSAC phosphodomain compared with that of the variant phosphodomain with inactive KI motifs.

We first determined the dependence of mitotic duration on the dosage of the variant phosphodomain with inactive KI motifs (M1-KI1*-KI2*-mNG-2xFkbp12; Figure 2A, left). The maximal response for this phosphodomain was higher than the previously defined maximal response for the eSAC phosphodomain containing the 12th MELT motif alone (211 vs. 157 min with $\pm 95\%$ confidence intervals of 169–357 and 152–163. Respectively, predicted by a four-parameter sigmoidal fit to the binned data). This difference likely results from different Bub1-Bub3 binding affinities of the first and 12th MELT motifs (Chen *et al.*, 2019). Interestingly, the phosphodomain with

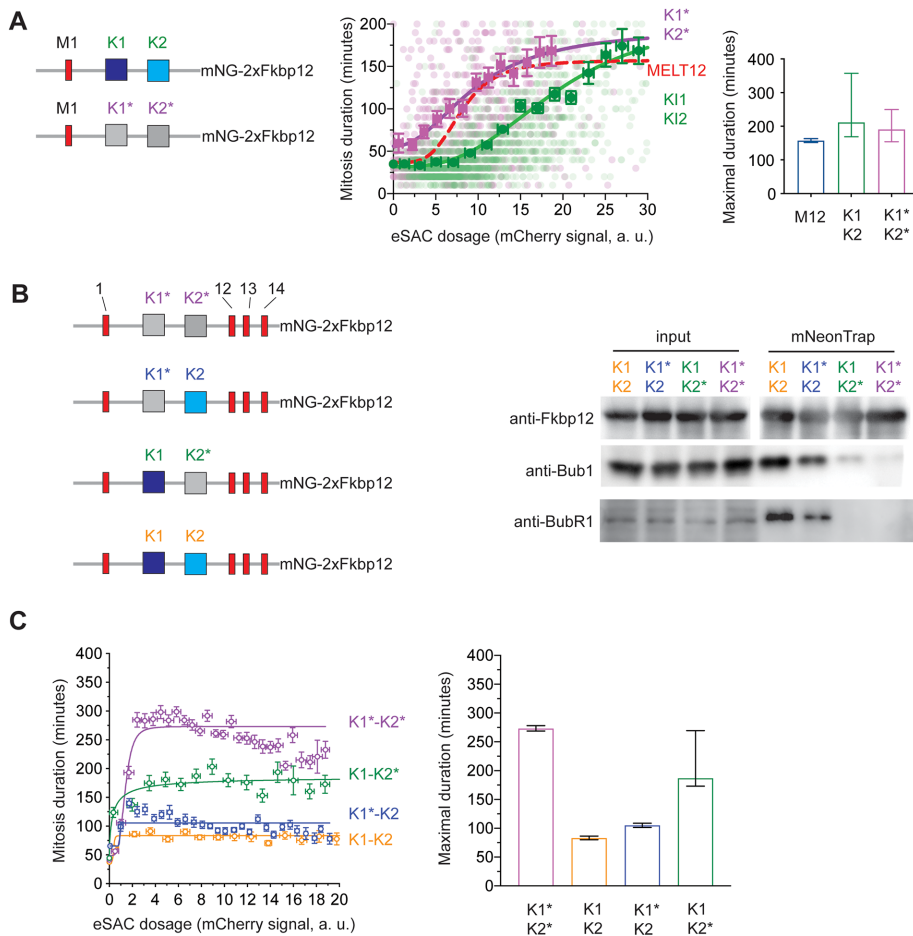


FIGURE 2: Characterization of the binding of the KI motifs in the eSAC phosphodomain with Bub1 and BubR1 and its contribution to eSAC signaling. (A) Left: Schematic of the two phosphodomains used to test whether the KI motifs contribute to MCC assembly mediated by the MELT motif in the eSAC phosphodomain. K11-K12 indicates phosphodomain with intact KI motifs; K11*-K12* indicates phosphodomains wherein the KI motifs are inactivated using suitable point mutations (see *Materials and Methods* for details). The scatter plot in the middle displays the dose-response data for the two phosphodomains ($n = 1888$ for K11-K12 [green] and $n = 836$ for K11*-K12* [magenta]) from ≥ 2 technical replicates; symbol usage follows the scheme established in Figure 1C. The bar graph on the right displays the maximal mitotic duration predicted by four-parameter sigmoidal fits to the binned mean values as in Figure 1C. Vertical lines display 95% confidence intervals on the fit parameter. (B) Left: Schematic of the phosphodomains consisting of four MELT motifs and either active or inactive (indicated by *) KI motifs. Right: Immunoprecipitation of the eSAC phosphodomains using mNeonGreen-Trap beads followed by immunoblot analysis to probe for the coimmunoprecipitate of the indicated proteins. This experiment was performed once. (C) Dose-response data for the indicated phosphodomains. Only the mean values of binned data are shown for clarity. Data analysis performed as in Figure 1D ($n = 1019$, 1024, 666, and 3219 from ≥ 2 technical replicates for K11-K12, K11-K12*, K11*-K12, and K11*-K12*, respectively). The bar graph on the right displays the maximal time in mitosis of the fitted maximal mitotic duration (error bars represent 95% confidence intervals).

active KI motifs (M1-K11-K12) has a significantly lower signaling strength: the eSAC concentration required for half-maximal response nearly doubled (half maximal effective concentration or $EC_{50} = 9.7$ and 19.4 a.u. respectively; Figure 2A, middle). The decreased signaling strength was eventually compensated by high eSAC dosage as evidenced by the maximal mitotic duration at high eSAC dosage (Figure 2A, middle and right). These data suggest that the Bub1 and BubR1 molecules recruited by the KI motifs do not enhance eSAC signaling mediated by the upstream MELT motif.

phosphodomains with only one MELT motif and the two KI motifs (Supplemental Figure S2A). These experiments show that the KI motifs interact with Bub1 and BubR1 constitutively; this interaction does not require the phosphorylation of MELT motifs. The experiments also confirm that the mutations significantly reduce Bub1 and BubR1 binding.

An N-terminal fragment of KNL1 spanning residues 1–334 localized transiently to prometaphase kinetochores, likely by interacting with kinetochore-bound Bub1 or BubR1 or with KNL1 itself

Bub1 and BubR1 interactions with the KI motifs do not require Mps1-mediated phosphorylation of KNL1

To better understand the observed suppression of eSAC activity by the KI motifs, we constructed a new phosphodomain by fusing an unstructured region of the Knl1 phosphodomain spanning three previously characterized MELT motifs (Knl1⁸⁸¹⁻¹⁰¹⁴) to the C-terminus of the phosphodomain used above (Knl1¹⁶⁰⁻²⁵⁶, also referred to as “M3”; see Figure 2B) (Vleugel et al., 2015; Chen et al., 2019). By incorporating multiple MELT motifs in the phosphodomain, we wanted to test whether the KI motifs influence the ability of the four MELT motifs in the phosphodomain to engage in synergistic signaling (Chen et al., 2019). On the basis of a previous study, we created mutant phosphodomains wherein the KI motifs were inactive individually or together (K11*-K12, K11-K12*, and K11*-K12*); the asterisk denotes a loss of function; Figure 2B) (Krenn et al., 2012).

We first determined whether the two KI motifs interact with Bub1 and BubR1 exclusively and whether the phosphorylation of MELT motifs is necessary for these interactions. We immunoprecipitated the four mNeonGreen-tagged eSAC phosphodomains from whole-cell extracts of mitotic HeLa cells in the absence of the Mps1 kinase domain using mNeonTrap beads and probed the precipitates for Bub1 and BubR1 (*Materials and Methods*). When both KI motifs were active (K11-K12), Bub1 and BubR1 coprecipitated with the eSAC phosphodomain. As expected, Bub1 and BubR1 did not coprecipitate with the eSAC phosphodomain containing inactive KI motifs (K11*-K12*); Figure 2B). Surprisingly, with the first KI motif inactive (K11*-K12), which interacts with Bub1 alone, Bub1 still coprecipitated with the phosphodomain, albeit at a lower level. Moreover, BubR1 coprecipitation was reduced. Inactivation of the second KI motif (K11-K12*) made BubR1 undetectable in the precipitate and reduced the amount of Bub1. These data can be explained by the heterodimerization between Bub1 and BubR1, although it remains possible that the second KI motif can interact with Bub1. We obtained similar results from immunoprecipitation experiments involving eSAC

(Kern *et al.*, 2015; Chen *et al.*, 2019). Therefore, we examined the localization of the K11-K12 and K11*-K12* phosphodomain in mitotic cells treated with rapamycin using immunofluorescence (Supplemental Figure S2B). Both phosphodomains colocalized with kinetochores, although the amount of kinetochore-localized K11*-K12* was ~20% lower than that of the K11-K12 phosphodomain (Supplemental Figure S2B). We next tested whether the kinetochore localization of the eSAC phosphodomains affects the dose-response data for the two phosphodomains indirectly, by affecting kinetochore-microtubule attachment. For this, we obtained dose-response data for the two phosphodomains while also observing chromosome congression and segregation in these two cell lines. For both cell lines, chromosome alignment appeared normal in most cells (Supplemental Videos 1 and 2). In the case of the K11*-K12* eSAC system, we observed lagging chromosomes in the spindle midzone and anaphase bridges in cells that underwent anaphase after a prolonged metaphase arrest (54 out of 403 cells). These defects can be ascribed to cohesion fatigue setting in during the metaphase arrest (Daum *et al.*, 2011). We also noted an increased incidence of unaligned or lagging chromosomes in cells with K11-K12 eSAC system (53 out of 373 cells examined, compared with 15 out of 403 cells for K11*-K12*) likely because the phosphodomain sequesters Bub1 and BubR1. To test whether the cells with chromosome missegregation affect the dose-response data, we revealed the dose-response trend by smoothing the data using LOWESS filtering by including and excluding the cells with chromosome segregation defects. The overall trend remained largely unaffected (Supplemental Figure S2C). Therefore, we conclude that the dose-response data of the eSAC systems are shaped mainly by the properties of the eSAC phosphodomain; they are minimally influenced by kinetochore-based SAC signaling.

Bub1 and BubR1 recruited by the KI motifs do not contribute to MCC assembly mediated by the MELT motifs

We first determined the baseline activity of the four MELT motifs by establishing the dose-response correlation for the eSAC phosphodomain with inactive KI motifs (K11*-K12* in Figure 2B, left, purple circles). The response elicited by this eSAC phosphodomain was nonmonotonic: the mitotic duration increased steeply before gradually decaying to a lower value (see Supplemental Figure S3A). A nonmonotonic response was not apparent for a previously characterized eSAC phosphodomain containing four MELT motifs (numbers 11–14) (Chen *et al.*, 2019). The different behaviors of the two phosphodomains may be ascribed to different Bub1-Bub3 binding affinities of the MELT motifs that they contain. Notably, when both KI motifs were active (K11-K12), the maximal duration of mitosis was significantly reduced (~87 min estimated by a four-parameter sigmoidal fit to the binned averages of the data; see Figure 2C). The KI motifs similarly suppressed the signaling strength of an extended phosphodomain containing seven MELT motifs (Supplemental Figure S3B).

We next determined the response elicited by the two eSAC phosphodomains containing four MELT motifs and only one active KI motif. When only the first KI motif was active (K11-K12*, only Bub1 depleted; see Figure 2B), the dose-response data were monotonic with a slightly lower maximal response than the maximal response elicited by K11*-K12* (Figure 2C, green circles and curve). When only the second KI motif was active (K11*-K12, Bub1, and BubR1 depleted; Figure 2C), the maximal response was significantly attenuated (blue circles and line in Figure 2C). Interestingly, the response to this eSAC was also nonmonotonic, an initial overshoot followed

by decay to a lower response level (residuals from the Hill equation fit shown in Supplemental Figure S3A).

These results reinforce the conclusion that Bub1 and BubR1 recruited by the two KI motifs do not directly contribute to MCC generation by the MELT motifs within the same phosphodomain (Figure 2C). The distinctly different effects of Bub1 and BubR1 sequestration on eSAC activity also suggest that the cellular abundance of these proteins may be an important aspect of SAC signaling (Heinrich *et al.*, 2013).

Numerical simulation of the dose-response data

The strong suppression of eSAC signaling by the second KI motif that binds BubR1 can be ascribed to two effects of BubR1 sequestration: the reduced rate of MCC assembly and a lowered limit on the maximal amount of MCC that can be generated. The latter effect is unlikely to play a major role in shaping the dose-response data. This is because the K11*-K12* eSAC delays mitosis by at most 300 min, significantly shorter than the ~1500-min-long arrest seen in nocodazole-treated HeLa cells (Collin *et al.*, 2013; Dick and Gerlich, 2013). Therefore, the amount of MCC produced by the eSAC systems is likely to be lower than the amount produced in nocodazole-treated HeLa cells. Therefore, a lower rate of MCC generation rather than a lower maximal amount of MCC that can be generated following BubR1 sequestration likely shapes the dose-response data.

An intuitive explanation for the dose-response dependence can be developed using the following four observations: 1) Bub1 and BubR1 interactions with the KI motifs do not require MELT motif phosphorylation (Figure 2B), 2) Bub1 and BubR1 recruited by the KI motifs do not contribute to the activity of the phosphorylated MELT motifs (Figure 2, A–C), 3) the eSAC phosphodomains are significantly more abundant than Bub1 and BubR1 (shown later), and 4) phosphorylated MELT motifs in an eSAC phosphodomain recruit Bub1, BubR1, and Mad1 (Chen *et al.*, 2019). The first three observations indicate that the two KI motifs in the eSAC phosphodomains will differentially sequester Bub1 or BubR1, and the last observation suggests that the MELT motifs in the eSAC phosphodomains will form two distinct signaling complexes: MELpT:Bub1:Mad1/2 and MELpT:Bub1:BubR1:Mad1/2 (Figure 3A; Cdc20 and Mad1/2 are present in both and hence are not indicated). When taken together, these observations suggest that the differential sequestration of Bub1 and BubR1 by the KI motifs will affect the composition of the signaling complexes assembled on the phosphodomains. If the two signaling complexes assemble the MCC at different rates, the result will be different mitotic delays, explaining why the four phosphodomains produce distinctly different maximal mitotic delays. The quantitative dose-response data and numerical simulations provide an excellent opportunity to test this model and the notion that MELpT:Bub1:BubR1:Mad1/2 generates MCC at a higher rate than the MELpT:Bub1:Mad1/2.

We simulated this model in two stages (Figure 3A). In the first stage, we calculate the equilibrium concentrations of the two signaling complexes using rates governed by mass action (Eqs. 6–15; *Materials and Methods*); in the second stage, we calculate the rate of MCC formation and its effect on the metaphase-to-anaphase transition (Eqs. 16 and 17; *Materials and Methods*). For both signaling complexes, the events before Mad2:Cdc20 formation are identical. Therefore, we did not explicitly simulate them. After this step, MELpT:Bub1:BubR1 can assemble the MCC either within the signaling complex itself or in the cytosol, whereas MELpT:Bub1 must rely on cytoplasmic MCC assembly. Using these insights, we expanded our previously described eSAC model (Chen *et al.*, 2019). This model simulates the activity of the four MELT motifs in a manner

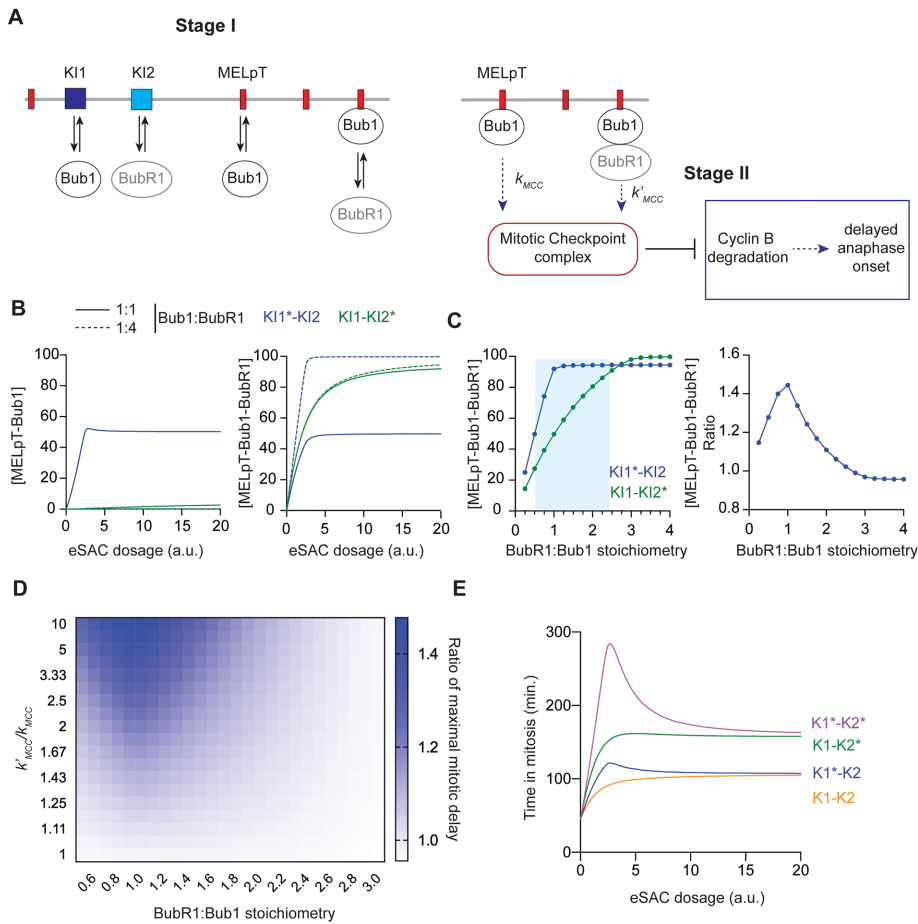


FIGURE 3: Numerical simulation of the dose-response data for the eSAC phosphodomains containing KI motifs. (A) Schematic of the two-stage model used to simulate the dose-response curves. (B) The influence of Bub1-BubR1 stoichiometry and the differential sequestration of Bub1 and BubR1 by the KI motifs on the equilibrium concentrations of the two signaling complexes formed on phosphorylated MELT motifs. (C) Comparison of the equilibrium concentration of the MELpT-Bub1-BubR1 complex assembled by K11*-K12 and K11-K12* (left) and the ratio (right) of their maximal responses as a function of the Bub1-BubR1 stoichiometry. For the two phosphodomains to generate different responses, the Bub1-BubR1 stoichiometry must be around 1:1 (indicated by the blue shaded area). (D) The ratio of the maximal responses produced by K11*-K12 and K11-K12* as a function of the Bub1-BubR1 stoichiometry and the ratio of the rates at which the MELpT-Bub1-BubR1 and the MELpT-Bub1 signaling complexes produce MCC (i.e., k_{MCC}^*/k_{MCC}). (E) Simulation of the dose-response curves for the four phosphodomains using the same set of parameter values.

analogous to that of the original model. Bub1-Bub3 and BubR1-Bub3 complexes are represented by “Bub1” and “BubR1” (Figure 3A) (Overlack *et al.*, 2015, 2017). Activities of the two KI motifs are simulated as protein-protein interactions assuming that K11 interacts only with Bub1 and K12 interacts only with BubR1 (Figure 3A). We further assume that the KI motifs and phosphorylated MELT motifs interact independently with the “Bub1” and “BubR1.” It is likely that Bub1 and BubR1 form bipartite interactions with the phosphodomain, for example, Bub1-Bub3 may bind simultaneously a MELT motif and the K11 motif. However, our simplifying assumption is reasonable given that the MELT motifs outnumber the KI motifs four to one (hence only one Bub1-Bub3 molecule can form such bipartite interaction) and because such bipartite interactions will mainly stabilize the MELpT:Bub1 signaling complex.

Phosphorylated MELT motifs strongly interact with the BubR1-Bub3 complex in vitro, and they have been suggested to contribute

to SAC signaling, although this observation and the ability of BubR1-Bub3 strongly bound to MELT to contribute to SAC signaling remains controversial (Overlack *et al.*, 2015; Zhang *et al.*, 2016). Furthermore, BubR1 engineered to bind strongly to phosphorylated MELT motifs does not support SAC function (Overlack *et al.*, 2015). These observations suggest that Bub1-BubR1 heterodimerization is primarily responsible for the enhancement seen in eSAC signaling. Finally, in vitro BubR1-Bub3 binds to the MELpT motifs with much higher affinity than the K12 motif ($K_D \sim 10$ and 450 nM, respectively) (Krenn *et al.*, 2012; Zhang *et al.*, 2016). Therefore, and because there are four MELT motifs and only one K12 motif in the eSAC phosphodomain, most of the BubR1 recruited to the phosphodomain will bind to MELpT motifs rather than the K12 motif. If this is the case, an activity of the K12 motif should not strongly affect the eSAC signaling activity. However, this prediction is not supported by the data. For these reasons, we assume that BubR1 does not bind to MELpT. As will be seen later, our model with these simplifying assumptions adequately captures the main features of the dose-response data.

Dependence of the equilibrium concentrations of MELpT:Bub1 and MELpT:Bub1:BubR1 assembled by the eSAC systems on Bub1-BubR1 stoichiometry

The equilibrium concentrations of MELpT:Bub1 and MELpT:Bub1:BubR1 depend on two sets of parameters: 1) the concentrations of Bub1, BubR1, and the eSAC phosphodomain (quantification shown after the simulations) and 2) the affinities of Bub1 and BubR1 for K11 and K12, respectively, Bub1 for phosphorylated MELT motifs and BubR1 for Bub1 (Krenn *et al.*, 2014; Vleugel *et al.*, 2015; Zhang *et al.*, 2016). We assume that Bub1-BubR1 heterodimerization occurs

after Bub1 binds MELpT. However, this assumption will not affect the behavior of the model. The values of the parameters used are listed in Supplemental Table S2.

Our first goal was to delineate the effects of the two KI motifs by understanding the reason for the different mitotic durations achieved by K11*-K12 and K11-K12* at high eSAC dosages. For these phosphodomains to elicit different maximal responses, they must form different amounts of MELpT:Bub1 and MELpT:Bub1:BubR1. Therefore, we investigated how the above two parameter sets affect the equilibrium concentrations of the two signaling complexes formed by K11*-K12 and K11-K12*. Given a set of affinities of K11 and K12 for Bub1 and BubR1, respectively, the concentrations of MELpT:Bub1 and MELpT:Bub1:BubR1 will depend on the relative cellular abundances of Bub1 and BubR1. If BubR1 is much more abundant than Bub1, then nearly every MELpT:Bub1 signaling complex will be able to recruit BubR1 to form MELpT:Bub1:BubR1.

Consequently, the concentration of MELpT:Bub1 will become negligible (dashed green and blue lines, respectively, near the X-axis in Figure 3B, left). At high eSAC dosage, the two eSAC systems will form similar amounts of MELpT:Bub1:BubR1 despite the differential sequestration of Bub1 and BubR1 (converging dashed lines at high eSAC dosage in Figure 3B, right). Therefore, their eSAC signaling activities will also be similar, contrary to our observations.

When BubR1 and Bub1 concentrations are similar, a sizable fraction of MELpT:Bub1 will not recruit BubR1 (Figure 3B, right, solid lines), especially at a high eSAC dosage. Therefore, at high eSAC dosage, the concentration of MELpT:Bub1:BubR1 is lower for KI1*-KI2 than for KI1-KI2* (solid lines in Figure 3B, left). Figure 3C shows how Bub1-BubR1 stoichiometry affects MELpT:Bub1:BubR1 concentration for the high and constant eSAC dosage (Figure 3C, left). BubR1:Bub1 <2.5 ensures that the two phosphodomains assemble different concentrations of MELpT:Bub1 and MELpT:Bub1:BubR1 (blue shaded region in Figure 3C, left). This difference in the equilibrium concentrations of the signaling complexes can explain the differential eSAC activities.

A higher rate of MCC generation by MELpT:Bub1:BubR1 compared with MELpT:Bub1 can explain the differential behavior of the two phosphodomains

Differences in the concentrations of MELpT:Bub1 and MELpT:Bub1:BubR1 will translate into different activities only if they generate MCC at different rates. As before, we calculate the rate of MCC generation by assuming it to be proportional to the concentrations of MELpT:Bub1 and MELpT:Bub1:BubR1 (Figure 3B). Following our experimental results, the KI-bound Bub1 and BubR1 do not promote eSAC signaling. To simulate the effect of the MCC generated on mitotic progression, we modified the model of metaphase-to-anaphase transition described by He *et al.* (Supplemental Figure S4B; *Materials and Methods*) (He *et al.*, 2011; Chen *et al.*, 2019).

As discussed in the preceding sections, the maximal mitotic duration produced by the two eSAC systems depends on 1) the equilibrium concentrations of MELpT:Bub1 and MELpT:Bub1:BubR1, which are in turn dependent on the Bub1-BubR1 stoichiometry, and 2) the values of the MCC generation rate constants k_{MCC} and k'_{MCC} . To determine the working combination of these factors, we fixed the eSAC dosage at a high value and calculated the duration of mitosis for a range of ratios of k_{MCC} to k'_{MCC} and Bub1:BubR1 stoichiometry. Figure 3D displays how the two ratios affect the maximal duration of mitosis achieved by KI1-KI2* and KI1*-KI2, respectively. For Bub1:BubR1 ~1 and $k_{MCC}/k'_{MCC} > 6$, the ratio of the maximal mitotic durations achieved by the KI1-KI2* and KI1*-KI2 eSAC systems exceeds 1.4.

Following this result, we used [Bub1]:[BubR1] = 1 and $k_{MCC}:k'_{MCC} = 0.1$ (rate constant for MCC assembly within the signaling complex is 10-fold higher than the rate constant for cytoplasmic MCC assembly) to simulate the dose-response curves for all four phosphodomains. This simulation captures key characteristics of the dose-response data for all four phosphodomains (Figure 3E). As before, the assumption of synergistic signaling was necessary to reproduce the nonmonotonicity of the dose-response data for the phosphodomain containing four MELT motifs (Chen *et al.*, 2019). Without it, the responses elicited by all phosphodomains become monotonic (Supplemental Figure S4D).

Stoichiometry of Bub1, BubR1, Mad1, and the eSAC phosphodomain in HeLa cells

The relative amounts of Bub1, BubR1, and the eSAC phosphodomain emerge as critical determinants of eSAC signaling. Therefore,

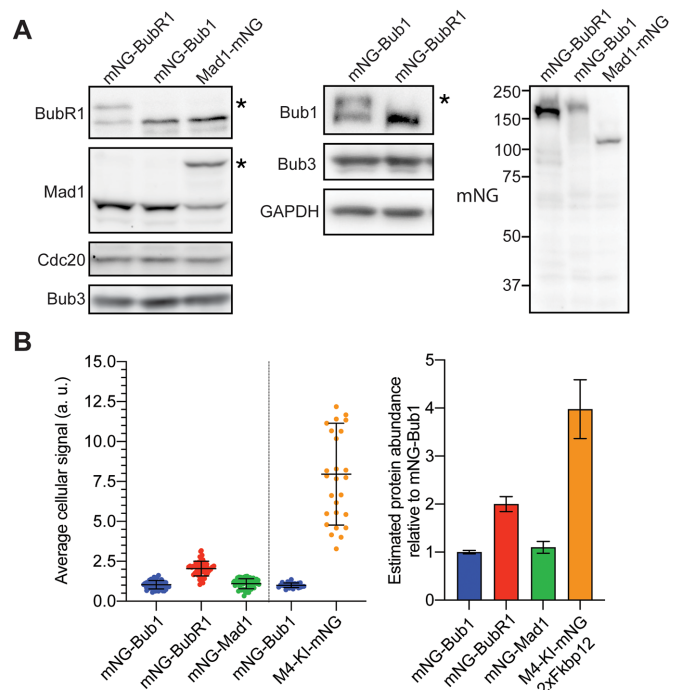


FIGURE 4: Quantification of the relative abundances of the eSAC phosphodomain, mNeonGreen-Bub1, mNeonGreen-BubR1, and Mad1-mNeonGreen in genome-edited HeLa cell lines.

(A) Immunoblots showing that roughly half of BubR1 and Mad1 (left) and Bub1 (middle) proteins in the three partially genome-edited cell lines is tagged with mNeonGreen (asterisks on the right of each displayed blot mark the mNG fusion protein). Right: Immunoblot of whole-cell extracts of the three cell lines probed with anti-mNeonGreen antibodies. This experiment was performed once. (B) Average mNG-Bub1, mNG-BubR1, Mad1-mNG, and M4-KI1-KI2-mNG-2xFkbp12 signals from mitotic HeLa cells (left) and estimation of the relative protein abundance, assuming that the total protein abundance is twice as high as the abundance of the mNG-labeled species (mean \pm SD; $n = 50$ each for mNG-Bub1, mNG-BubR1, and Mad1-mNG, $n = 27$ for M4-KI-mNG-2xFkbp12).

for comparative protein abundance measurements, we constructed genome-edited HeLa cell lines wherein mNeonGreen (abbreviated as mNG) was fused to the N-terminus of Bub1 and BubR1 and the C-terminus of Mad1. In all three cases, we obtained heterozygous cell lines with partially edited genomes. Consequently, approximately half of the protein in these cells was labeled (Figure 4A; *Materials and Methods*).

Quantitation of mNG fluorescence in mitotic cells revealed that the KI1-KI2 phosphodomain was two- to fourfold more abundant than the three SAC proteins (Figure 4B; *Materials and Methods*). Therefore, and given the constitutive activity of the two KI motifs, the eSAC phosphodomains containing active KI motifs will deplete Bub1 and BubR1 from the cytosol. The measurements also show that BubR1 is approximately twofold more abundant than Bub1 and Mad1 (Figure 4B). In the case of BubR1, the measured abundance includes free BubR1-Bub3 and BubR1-Bub3 incorporated into MCC. Although the fraction of free BubR1-Bub3 remains unknown, this value is likely to be less than twofold higher than that of Bub1-Bub3, consistent with the requirement of comparable amounts of Bub1-Bub3 and BubR1-Bub3 in our simulations.

Recruitment of BubR1 by Bub1 per se strengthens kinetochore-based SAC signaling

Following these results and insights, we reexamined the role of Bub1-BubR1 heterodimerization in kinetochore-based SAC signaling. PP2A recruitment to the kinetochore in this manner contributes to SAC silencing directly (Kruse *et al.*, 2013; Espert *et al.*, 2014; Qian *et al.*, 2017) and indirectly by either promoting Protein Phosphatase 1 recruitment (Nijenhuis *et al.*, 2014) or stabilizing kinetochore-microtubule attachment (Suijkerbuijk *et al.*, 2012). We confirmed these findings using the knock-in/knockdown strategy wherein endogenous BubR1 was knocked down using RNA interference (RNAi) and replaced with fluorescently tagged versions of either wild-type BubR1 or BubR1 lacking the heterodimerization domain (BubR1^{ΔHD}; Supplemental Figure S5A). In media containing 100 nM GSK923295 (a small molecule inhibitor of the mitotic kinesin CENP-E), mCherry-BubR1^{ΔHD} expression prolonged mitosis compared with mCherry-BubR1 expression (Supplemental Figure S5B), because the reduced BubR1 recruitment to the kinetochore also reduced PP2A activity as shown previously (Kruse *et al.*, 2013; Overlack *et al.*, 2015; Hertz *et al.*, 2016; Zhang *et al.*, 2016). Knockdown of the five isoforms of the PP2A-targeting subunit B56 in addition to BubR1 in these experiments did not affect the results, indicating that the phenotype was not caused by the activity of any residual BubR1 (Supplemental Figure S5B) (Foley *et al.*, 2011).

To separate the effect of BubR1 recruitment to the kinetochore from the BubR1-mediated recruitment of PP2A, we created two additional BubR1 mutants: mNG-BubR1^{ΔKARD} that lacks the PP2A-binding KARD domain and mNG-BubR1^{ΔHD, ΔKARD} that lacks the KARD domain and the BubR1 heterodimerization domain (Figure 5A). The complete removal of the KARD domain will abolish the binding of B56α and other isoforms of B56 onto BUBR1 (Wang *et al.*, 2016a,b), enabling us to analyze whether the recruitment of BUBR1 to the signaling kinetochore per se contributes to the SAC activity. Importantly, we ensured that the expression level of these mutants was similar to that of wild-type BubR1 because the transient overexpression of BubR1 can deplete the cytosolic pool of Bub3 (Taylor *et al.*, 1998) and adversely affect the SAC or induce cell death (unpublished data). Higher cytosolic BubR1 concentration may also proportionally increase the rate of cytosolic MCC formation and thus mask impaired MCC assembly within the kinetochore.

We knocked down endogenous BubR1 in HeLa-A12 using RNAi and rescued these cells with mNG-BubR1^{ΔKARD} or mNG-BubR1^{ΔHD, ΔKARD}. As expected, mNG-BubR1^{ΔKARD} localized to unattached kinetochores, whereas mNG-BubR1^{ΔHD, ΔKARD} localization to unaligned kinetochores was undetectable (Figure 5B). We also quantified the duration of mitotic arrest using nocodazole treatment following the previous studies. To ensure that the BubR1 mutants were not overexpressed, we established the physiological BubR1 expression level by quantifying cytosolic BubR1 fluorescence in the genome-edited mNG-BUBR1 HeLa-A12 cells treated with control small interfering RNA (siRNA) and imaged under identical conditions. In our knock-in/knockdown experiments, we considered only those cells exhibiting mNG intensity that is 0.5–2 times the average mNG intensity of mitotic mNG-BubR1 HeLa-A12 cells (Figure 5C, left). Quantification of mitotic duration revealed that cells expressing mNG-BubR1^{ΔKARD} arrested significantly longer than control cells; the longer duration is attributable to the loss of PP2A activity from the kinetochores (Saurin *et al.*, 2011). Notably, cells rescued with mNG-BubR1^{ΔHD, ΔKARD} arrested for a significantly shorter amount of time compared with the cells rescued with mNG-BubR1^{ΔKARD} (Figure 5C, right). Thus, the recruitment of BubR1 per se strengthens the SAC.

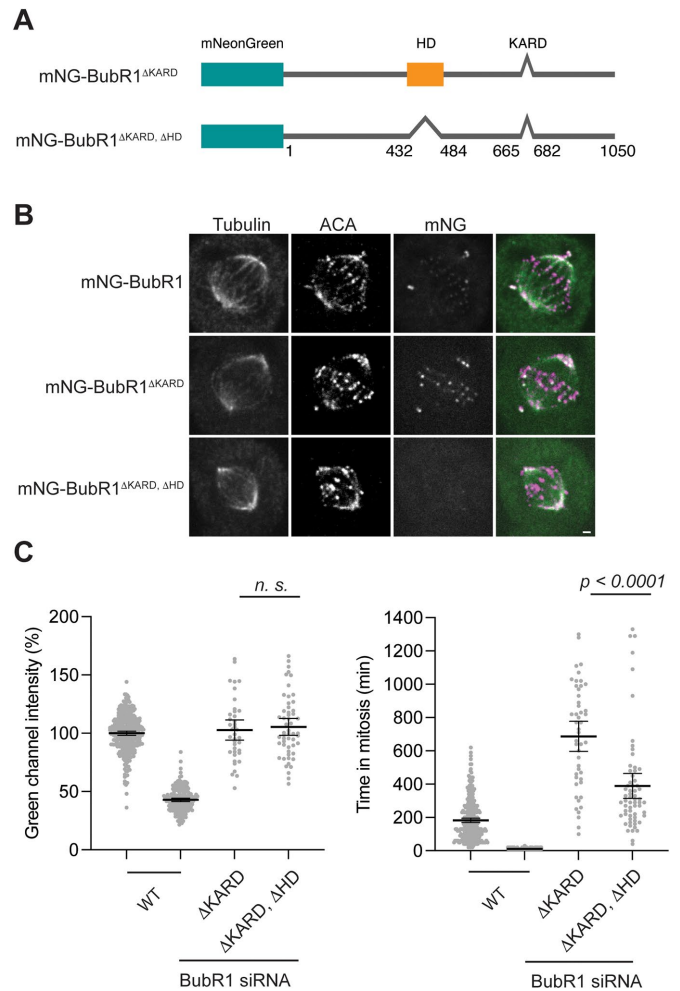


FIGURE 5: Recruitment of BubR1 by Bub1 per se contributes to the activity of the kinetochore-based SAC signaling. (A) Schematic domain organization for the two new BubR1 mutants. (B) Micrographs of representative cells displaying the indicated antigens at the top. The top row displays micrographs of the partially genome-edited cell line expressing mNG-BubR1. The bottom two rows display representative cells after endogenous BubR1 was knocked down and the indicated mutant, mNG-tagged version was ectopically expressed (scale bar ~ 1.22 microns). (C) Left: The duration of mitosis of either genome-edited mNG-BUBR1 or cells that ectopically expressed the indicated BubR1 mutant after treatment with BubR1 siRNA in media containing 25 nM nocodazole. Scatterplot on the right displays the average cytosolic mNeonGreen signal from the same cells ($n = 347, 194, 48,$ and $63,$ respectively, from two technical replicates; horizontal lines indicate mean \pm 95% confidence intervals). The p value was obtained from Welch's t test performed in GraphPad Prism.

In conclusion, Bub1-BubR1 heterodimerization significantly enhances SAC signaling activity in human cells. This enhancement can be simply due to enrichment of BubR1 at the site of formation of Mad2-Cdc20 (Lara-Gonzalez *et al.*, 2021a; Piano *et al.*, 2021), although more complicated mechanisms can also be envisioned. Bub1 and BubR1 recruitment via the KI motifs does not contribute to eSAC signaling mediated by MELT motifs, indicating that their contribution to SAC signaling is likely to be minor. Although prior studies found that the KI motifs promote SAC signaling, this contribution was detectable only in the context of recombinant Kn1 variants containing either just one MELT motif (Krenn *et al.*, 2014) or three inactive MELT motifs (Vleugel *et al.*, 2013); the contribution

was undetectable in a Knl1 variant containing multiple MELT motifs but lacking the N-terminus including the KI motifs (Zhang *et al.*, 2014). These observations can be explained by the KI motifs' relatively weak affinity for the TPR domains of Bub1 and BubR1 (Bolanos-Garcia *et al.*, 2011; Krenn *et al.*, 2012) compared with the affinity of phosphorylated MELT motifs for the Bub1-Bub3 complex (Primorac *et al.*, 2013) and the fact that MELT motifs outnumber the KI motifs. Owing to these factors, the phosphorylated MELT motifs likely recruit the majority of Bub1 and BubR1 to the kinetochore (Zhang *et al.*, 2014; Overlack *et al.*, 2015; Vleugel *et al.*, 2015).

Our findings highlight the dual effect of Bub1-mediated BubR1 recruitment on the SAC. BubR1 stabilizes the kinetochore-microtubule attachment by recruiting PP2A, thereby promoting the silencing of SAC. But it also promotes the SAC activity per se, which is critical for minimizing chromosome missegregation in normally dividing cells, wherein the last few unattached kinetochores need to be able to signal the cell to delay anaphase onset (Roy *et al.*, 2020).

MATERIALS AND METHODS

[Request a protocol](#) through *Bio-protocol*.

Plasmid construction

The plasmids used for the stable cell lines were based on plasmids that have been described previously (Chen *et al.*, 2019). Briefly, the phosphodomain was integrated into either *NotI* or *Ascl* and *XhoI* restriction sites to create constitutively expressed phosphodomain-mNeonGreen-2xFkbp12. The Mps1⁵⁰⁰⁻⁸⁵⁷ fragment corresponding to the Mps1 kinase domain was integrated into the *FseI* and *BglII* restriction sites to create conditionally expressed Frb-mCherry-Mps1⁵⁰⁰⁻⁸⁵⁷.

eSAC phosphodomains spanning the 1st MELT motif (M1) and the two KI motifs were created by fusing Knl1¹⁶⁰⁻²⁵⁶ to mNeonGreen-2xFkbp12. eSAC phosphodomains containing four MELT motifs and the two KI motifs were created by fusing Knl1¹⁶⁰⁻²⁵⁶ to Knl1 fragment Knl1⁸⁸¹⁻¹⁰¹⁴ spanning MELT motifs 12–14, which has been characterized previously (Vleugel *et al.*, 2015). The activity of the first KI motif was disrupted by changing its amino acid sequence from "KIDTTS-FLANLK" to "KADAASALANLK" (KI1*). Similarly, the activity of the second KI motif was disrupted by mutating its amino acid sequence from "KIDFNDFIKRLK" to "KIDFNDAIKALK" (KI2*) following Krenn *et al.* (2012). The relevant open reading frames in all plasmids were confirmed using Sanger sequencing.

DNA repair templates used for CRISPR/Cas9-mediated genome editing were constructed via DNA assembly using the NEB HiFi DNA assembly kit per the manufacturer's instructions. Successfully edited alleles encode mNeonGreen-tagged SAC proteins that separate the corresponding wild-type protein and the fluorescent protein mNeonGreen by a short flexible linker (mNG-BUBR1 and mNG-BUB1: GSGGSG; MAD1-mNG: GGAGGSGG). The sequences of all homology-directed repair template plasmids and Cre-lox recombination-mediated cassette exchange plasmids are available upon request.

Tissue culture and cell line construction for eSAC analyses

HeLa cells were grown in DMEM supplemented with 10% fetal bovine serum (FBS), 1% Pen/Strep, 1×-GlutaMAX, and 25 mM HEPES under standard tissue culture conditions (37°C and 5% CO₂). Stable cell lines expressing the two eSAC components were generated by integrating a bicistronic eSAC plasmid at engineered *lox* sites in the HeLa genome according to the protocol described in Khandelia *et al.* (2011). Upon transfection, DMEM supplemented with 1 µg/ml puromycin was used to select transformed cells, and all the colonies were

pooled to culture the transformed cells used in the experiments. The expression of the eSAC components in each cell line was confirmed using immunoblotting with FKBP12 and mCherry antibodies.

For dose-response analysis, each eSAC cell line was plated ~40–48 h before the start of the experiment in DMEM without puromycin. Doxycycline was added at the time of plating to induce the expression of Frb-mCherry-Mps1. Before imaging, the cells were washed with phosphate-buffered saline (PBS). Fluorobrite media with 10% FBS, 1% Pen/Strep with or without rapamycin were added to each well.

Genome editing HeLa cells using CRISPR/Cas9

The guide RNAs (gRNAs) for in situ BUBR1 and BUB1 N-terminal mNeonGreen-tagging were 5'-CAGGAUGGCGGCGGUGAAGA-3' and 5'-GGUUCAGGUUUGGCCGUCG-3', respectively. The gRNA for in situ MAD1 C-terminal mNeonGreen-tagging was 5'-CAGAC-CGUGGCGUAGCCUGC-3'. Single-guide RNAs (sgRNAs) were synthesized using the EnGen sgRNA Synthesis Kit (for the *Streptococcus pyogenes*-originated Cas9; New England Biolabs). The SpCas9-sgRNA ribonucleoprotein (RNP) complex was assembled at room temperature in a buffer consisting of 20 mM HEPES-KOH (pH 7.5), 150 mM KCl, 1 mM MgCl₂, 10% (by volume) of glycerol, and 1 mM dithiothreitol using 100 pmol of SpCas9- 2 × NLS (the QB3 MacroLab) and 120 pmol of sgRNA. The RNP complex and 1.5 µg of a linearized homology-directed repair template plasmid were transfected into 2 × 10⁵–5 × 10⁵ nocodazole-arrested mitotic HeLa A12 cells using a Nucleofector and the associated Cell Line Kit R (Lonza) following the manufacturer's instructions. After 5 wk, green fluorescent-positive mitotic cells (arrested by 330 nM nocodazole for 16 h) were sorted directly into 96-well plates at 1 cell/well. Healthy colonies were subject to further validation by genotyping and sequencing, as well as immunoblotting.

For genotyping, HeLa-A12 genomic DNAs were purified using the Wizard SV Genomic DNA Purification System (Promega). Genotyping primers (BUBR1 forward primer 5'-CCTGGTCACATCT-GAGCTAT-3', BUBR1 reverse primer 5'-CTCAGTGAGACTCCAGT-GTT-3', BUB1 forward primer 5'-CCCTCTACATGAAGGCGCTA-3', BUB1 reverse primer 5'-GCTCGCCCAAGGTAACATT-3', MAD1 forward primer 5'-GGACTTTTCAGGGACGTGGT-3', and MAD1 reverse primer 5'-GAGTTGGGAGGAGGGGACTC-3') were designed to bind outside of homology arms to avoid false-positive colonies from integration of the homology-directed repair template plasmid to an off-target genomic locus.

Drug and RNAi treatments

To induce the expression of the mCherry-Frb-Mps1 kinase domain doxycycline was added to a final concentration of 2 µg/ml (stock concentration 2 mg/ml in dimethyl sulfoxide [DMSO]) ~48 h before the start of the experiment. Before the start of each experiment, rapamycin was added ~1 h prior to imaging to a final concentration of 500 nM (stock concentration 500 µM in DMSO) to induce the dimerization of the eSAC kinase domain with the eSAC phosphodomain. Nocodazole was added to a final concentration of 330 nM (stock concentration 330 µM in DMSO). The cocktail of siRNA against five different B56 isoforms was added to a final concentration of 40 nM (stock concentration 10 µM).

The siRNA sequences were obtained from Zhang *et al.* (2016). siRNA sequences used to knock down B56 isoforms were obtained from Foley *et al.* (2011). Cell cycle synchronization in G1/S was achieved by treating cells with 2.5 mM thymidine (from a 100 mM stock in PBS) for 16–18 h. Cells were washed with DMEM for release from the G1/S arrest. To arrest cells in a prometaphase-like condition,

cells were released from a G1/S block and then treated with 236 nM GSK923295 (stock concentration 236 μ M in DMSO) ~7 h postrelease and imaged after 1 h.

Immunoprecipitation

HeLa A12 cells constitutively expressing either MELT1-KI or MELT1-KI-M3 were synchronized at G1/S by 2.5 mM thymidine. Cells were synchronized in metaphase using 10 μ M MG132 nine hours after being released from a (double) thymidine block. After another 1.5 h, cells were scraped off the plate, washed once with PBS, pelleted, snap-frozen, and stored at -80°C . Cells were thawed, resuspended in the complete lysis buffer (75 mM HEPES-HCl [pH 7.5], 150 mM KCl, 1.5 mM EGTA, 1.5 mM MgCl_2 , 10% [by volume] glycerol, and 0.075% [by volume] Nonidet P-40 [AmericanBio]; immediately before use one cOmplete protease inhibitor cocktail tablet [EDTA-free; Roche Diagnostics] and a phosphatase inhibitor cocktail [1 mM $\text{Na}_4\text{P}_2\text{O}_7$, 0.1 mM Na_3VO_4 , 5 mM NaF, and 2 mM sodium β -glycerophosphate]) and lysed for 1 h at 4°C while rotating. Cell lysates were then centrifuged at $18,000 \times g$ for 25 min at 4°C . The supernatant was subsequently cleared by control agarose beads for 1.5 h at 4°C to reduce nonspecific binding. Cleared supernatant was then mixed with mNeonGreen-Trap agarose beads (ChromoTek) and rotated for 1.5 h at 4°C . Beads were washed four times using the lysis buffer. Finally, 2 \times Laemmli buffer (Bio-Rad Laboratories) supplemented with β -mercaptoethanol was added to the beads. Samples were boiled in a water bath for 10 min before being subjected to SDS-PAGE.

The following antibodies and working dilutions were used in immunoblotting: SB1.3 antibody against: BUB1 (Taylor *et al.*, 2001), 1:500 or 1:1000, sheep polyclonal; BUB3 (Sigma B7811), 1:500, rabbit polyclonal; FKBP12 (Abcam ab2918), 1:2000, rabbit polyclonal; BUBR1 (Bethyl A300-995A), 1:1000, rabbit polyclonal; and mNeonGreen (ChromoTek 32F6) 1: 500.

Immunofluorescence

HeLa cell lines were grown on sterile coverslips in six-well plates in media supplemented with 1 $\mu\text{g}/\text{ml}$ doxycycline to induce the expression of the mCherry-Frb-Mps1 kinase domain. After ~48 h, the cells were treated with 500 nM rapamycin. After 4 h of incubation, cells were fixed with 4% paraformaldehyde and stained with ACA antibodies (1:1000; Antibodies Inc., Davis, CA) and Alexa-633-conjugated secondaries (1:5000). After staining, the cells were embedded in Diamond mounting media and stored at room temperature.

The mounted cells were imaged on an Eclipse Ti-E/B inverted microscope (Nikon) with a CFI Plan Apochromat VC 100 \times , 1.40 NA oil objective (Nikon). The microscope was equipped with a H117E1 motorized stage (Prior Scientific), a NanoScanZ 100 piezo stage (Prior Scientific), and an X-Light V2 L-FOV confocal unit with 60 μm pinholes (CrestOptics). A CELESTA Light Engine (Lumencor) served as the excitation laser source, featuring a 477-nm line for imaging the mNeonGreen protein, a 546-nm line for imaging mCherry, and a 647-nm line for imaging the Alexa-633-conjugated antibodies. Fluorescence emission light was filtered by ET605/52m (Chroma Technology) for the red channel and by ET525/36m (Chroma Technology) for the green channel. Images were acquired by a Prime 95B 25 mm sCMOS camera (Teledyne Photometrics). A custom MATLAB program was used to quantify kinetochore-localized fluorescence signals.

Long-term, live-cell imaging of HeLa cells

Imaging was conducted as described in detail previously (Chen *et al.*, 2019). We used either the Incucyte Zoom live cell imaging

system (Sartorius) or the ImageXpress Nano live cell imaging system (Molecular Devices), both equipped with a 20 \times phase objective. To image cells on the Incucyte system, cells were plated in 12-well plastic tissue culture plates, whereas they were plated in 24-well plate glass-bottom dishes (Corning) for the ImageExpress Nano system. At each position, one phase, GFP, and mCherry image was acquired every 10 min. The exposure times for mCherry and GFP images were adjusted to minimize photobleaching while enabling accurate determination of intensity values. It should be noted that the excitation sources, optics, and detector on the ImageXpress Nano and the Incucyte microscope are entirely different. Therefore, the mCherry intensity values across different experiments are not directly comparable.

Image analysis

Before intensity quantification, acquired images were preprocessed using functions from the "Image Processing Toolbox" provided with MATLAB as follows. First, the phase image sequence was registered to remove any movement of the field of view between adjacent time points, and at each time point, the same transform was applied to the GFP and mCherry images to register them. Additionally, image intensity from a blank, unseeded well was used for background correction of the fluorescence channels. Next, GFP and mCherry fluorescence signals were quantified using a custom graphical user interface (GUI) written in MATLAB as described previously. Briefly, this interface uses cross-correlation of each phase image with a circular kernel to identify cells with circular shapes close to the diameter of the circular kernel. The centroids of these shapes were then linked along the time axis. These images were presented to the user via the GUI to 1) discard false-positive, nonmitotic cells or debris and 2) visually correct the time of entry into or exit from mitosis. The GUI then calculated the GFP and mCherry signals per cell as the average fluorescence intensity.

In all the dose-response assays discussed in this study, the phosphodomain is highly and constitutively expressed in all cells, whereas the kinase domain is expressed conditionally by an inducible promoter. Consequently, the amount of the kinase domain expressed varies from cell to cell, and it is lower than the amount of the phosphodomain in most cells. Because of this design of the eSAC system, the dosage of the dimerized signaling complex in a cell can be inferred from the amount of Frb-mCherry-Mps1⁵⁰⁰⁻⁸¹⁷ in that cell. Therefore, we defined the dosage of the eSAC signaling complex by quantifying the average mCherry fluorescence within a cell and the response as the duration of mitosis (the amount of time that the cell spends with a spherical morphology that is characteristic of mitotic HeLa cells).

The Hill equation is used to fit the sigmoidal trend:

$$\text{Time in mitosis} = m + \frac{M}{1 + \left(\frac{\text{EC50}}{[\text{eSAC activator}]} \right)^n}$$

wherein n is the Hill coefficient and EC50 is the level of the eSAC activator at which the time in mitosis reaches the middle between the baseline level (m) and the plateau level ($m + M$).

Statistical analysis

To determine the overall trend in the dose-response data, the data were first binned (in MATLAB), and then the mean values of each bin were overlaid on the data. The number of observations and technical replicates are noted in the figure legends. These mean values

were fitted with a four-parameter sigmoidal curve using GraphPad Prism 9 software. The statistical significance of the difference between the mean values in Figure 5C and Supplemental Figure S5 was assessed using the unpaired t test with Welch's correction. LOWESS filtering of the data in Supplemental Figure S2C was performed using GraphPad Prism with 20 points in the smoothing window.

MATHEMATICAL MODELING

Modeling the activity of Bub1 phosphodomains

Stage 1: Calculation of the steady-state concentrations of signaling complexes. (MATLAB codes available on GitHub: <https://github.com/anandban/eSAC-KI>).

This model simulates the eSAC activity of the Bub1²²¹⁻⁶²⁰ and Bub1⁴⁴¹⁻⁶²⁰ phosphodomains. In the equations below, we refer to these phosphodomains simply as "Bub1." The eSAC activator complex is formed by the dimerization of Bub1 with the Mps1 kinase domain (Bub1:Mps1). Once Mps1 phosphorylates Bub1, Bub1 can bind Mad1/2 (Bub1:Mps1:Mad1/2). Therefore, the concentrations of different species of Bub1 are related by the equation

$$[\text{Bub1}]_T = [\text{Bub1:Mps1:Mad1/2}] + [\text{Bub1:Mps1}] + [\text{Bub1}] \quad (1)$$

Assuming reversible binding between phosphorylated Bub1 and Mad1/2 complex, the concentration of eSAC activator complex will saturate to a value dependent on the finite concentration of Mad1/2 (set at 100 nM; Supplemental Figure S1A). Note that Bub1 can produce MCC only if it recruits Mad1/2. Therefore, even though Bub1:Mps1 and Bub1 can both bind BubR1 and Cdc20, they do not participate in SAC signaling. The recruitment of SAC proteins, formation of signaling complexes, and MCC are calculated by assuming mass action kinetics.

Model of Bub1-mediated MCC formation. Available data suggest that a signaling complex comprising Bub1²²¹⁻⁶²⁰, BubR1, Mad1, and Cdc20 facilitates the formation of either Mad2:Cdc20 or the MCC. We assume that when BubR1 is present the phosphodomain assembles MCC and when BubR1 is absent the phosphodomain produces Mad2:Cdc20. Therefore, the rate of Mad2:Cdc20 and MCC formation is calculated as

$$\begin{aligned} &\text{Mad2:Cdc20 formation rate at the Bub1}^{231-620} \text{ phosphodomain} \\ &= k_{\text{asmcc2}} \cdot [\text{Mad2}]_i \cdot [\text{Cdc20:Bub1:Mad1/2}] \end{aligned} \quad (2)$$

$$\begin{aligned} &\text{MCC formation rate at the Bub1}^{231-620} \text{ phosphodomain} \\ &= k_{\text{asmcc2}} \cdot [\text{Mad2}]_i \cdot [\text{Cdc20:Bub1:Mad1/2:BubR1}] \end{aligned} \quad (3)$$

where $[\text{Mad2}]_i$ = the concentration of inactive (open) form of Mad2 in the cytoplasm; $[\text{Cdc20:Bub1:Mad1/2}]$ = the concentration of the complex between Bub1, Mad1, and Cdc20; and $[\text{Cdc20:Bub1:Mad1/2:BubR1}]$ = the concentration of the complex between Bub1, BubR1, Mad1, and Cdc20.

For the sake of simplicity, we assume that the rate constant for MCC formation (k_{asmcc2}) is numerically equal to the rate constant for Mad2:Cdc20 formation. This assumption is consistent with the observation that Mad2:Cdc20 formation is the rate-limiting step in MCC formation (Faesen *et al.*, 2017).

The cytosolic Mad2:Cdc20 molecules produced by either phosphodomain interact with cytosolic, free BubR1 to complete MCC formation. We denote the rate constant for this reaction by k_{asmcc1} . Therefore, the rate of cytosolic MCC formation is calculated as

$$\begin{aligned} &\text{MCC formation rate in the cytoplasm} \\ &= k_{\text{asmcc1}} \cdot [\text{BubR1}]_f \cdot [\text{Mad2:Cdc20}] \end{aligned} \quad (4)$$

where $[\text{BubR1}]_f$ = the concentration of free BubR1 in the cytoplasm.

Stage 2: Effect of MCC formation on the timing of metaphase-to-anaphase transition. We used a previously described model of metaphase-to-anaphase transition to simulate the effect of the MCC generated on the duration of mitosis (He *et al.*, 2011; Chen *et al.*, 2019). In this model (schematic at the top of Supplemental Figure S1B), cyclin B ("CycB") is synthesized at a constant rate and degraded upon APC:Cdc20-dependent ubiquitination (denoted simply as Cdc20). The abundance of CycB determines the activity of CDK1:CycB complexes, which in turn determines the activity of the eSAC complexes via phosphorylation. CDK1:CycB activity is antagonized by the counteracting protein phosphatase PP2A:B56 ("CAPP") (Sullivan *et al.*, 2004; Bouchoux and Uhlmann, 2011). This scheme is consistent with recent data revealing that CDK1:CycB phosphorylates Bub1 to promote its interaction with Mad1 (Ji *et al.*, 2017). Furthermore, Mps1 kinase activity is also down-regulated by PP2A (Espert *et al.*, 2014; Hayward *et al.*, 2019). This scheme regulates the amount of active eSAC.

The active eSAC ultimately produces MCC according to the scheme discussed in detail above with BubR1 as an MCC component. Therefore, we modified the original model to include BubR1 as well as the dissociation of MCC into its constituent proteins (shown by the red dashed arrow in Supplemental Figure S1B). Furthermore, active APC:Cdc20 promotes the inactivation of closed/active Mad2 in MCC; this positive feedback of active Cdc20 on its own release from the MCC accelerates the activation of APC:Cdc20 during the transition into anaphase (He *et al.*, 2011; Chen *et al.*, 2019).

The equations for this model are given below using the following notation:

$$\text{eS1} \sim \text{Bub1:Mps1:Mad1/2} \quad \text{and}$$

$$\text{eS2} \sim \text{Bub1:Mps1:Mad1/2:Bub1:BubR1}$$

$$\begin{aligned} \frac{d[\text{eS1}:\text{Cdc20}]}{dt} &= k_{\text{fcdc}} [\text{eS1}] \cdot [\text{Cdc20}] - k_{\text{rcdc}} [\text{eS1}:\text{Cdc20}] \\ &+ k_{\text{dies2}} [\text{eS2}:\text{Cdc20}] + k_{\text{dies2}} [\text{eS2}_A:\text{Cdc20}] \end{aligned} \quad (5a)$$

$$\begin{aligned} \frac{d[\text{eS1}_A]}{dt} &= k_{\text{ancyc}} [\text{eS1}] \cdot [\text{CycB}] - k_{\text{incapp}} [\text{eS1}_A] \cdot [\text{CAPP}] \\ &- k_{\text{ases2}} [\text{eS1}_A] \cdot [\text{BubR1}] + k_{\text{dies2}} [\text{eS2}_A] - k_{\text{fcdc}} [\text{eS1}] \cdot [\text{Cdc20}] \\ &+ k_{\text{rcdc}} [\text{eS1}_A:\text{Cdc20}] + k_{\text{asmcc2}} [\text{eS2}_A:\text{Cdc20}] \cdot \text{Mad2I} \\ &+ k_{\text{asc1}} [\text{eS1}_A:\text{Cdc20}] \cdot \text{Mad2I} \end{aligned} \quad (5b)$$

$$\begin{aligned} \frac{d[\text{eS1}_A:\text{Cdc20}]}{dt} &= k_{\text{fcdc}} [\text{eS1}_A] \cdot [\text{Cdc20}] - k_{\text{rcdc}} [\text{eS1}_A:\text{Cdc20}] \\ &- k_{\text{asc1}} [\text{eS1}_A:\text{Cdc20}] \cdot \text{Mad2I} \end{aligned} \quad (5c)$$

$$\begin{aligned} \frac{d[\text{eS2}_I]}{dt} &= -k_{\text{ancyc}} [\text{eS2}_I] \cdot [\text{CycB}] + k_{\text{incapp}} [\text{eS2}_A] \cdot [\text{CAPP}] \\ &- k_{\text{fcdc}} [\text{eS2}_A] \cdot [\text{Cdc20}] + k_{\text{rcdc}} [\text{eS2}_I:\text{Cdc20}] \end{aligned} \quad (5d)$$

$$\begin{aligned} \frac{d[eS2_I : Cdc20]}{dt} = & -k_{dies2} [eS2_I : Cdc20] + k_{fcdc} [eS2_I] \cdot [Cdc20] \\ & - k_{rcdc} [eS2_I : Cdc20] \end{aligned} \quad (5e)$$

$$\begin{aligned} \frac{d[eS2_A]}{dt} = & k_{ases2} [eS1_A] \cdot [BubR1] - k_{dies2} [eS2_A] + k_{ancyc} [eS2_I] \cdot [CycB] \\ & - k_{incapp} [eS2_A] \cdot [CAPP] - k_{fcdc} [eS2_I] \cdot [Cdc20] \\ & + k_{rcdc} [eS2_A : Cdc20] + k_{asc1p} [eS2_A] \cdot Mad21 \end{aligned} \quad (5f)$$

$$\begin{aligned} \frac{d[eS2_A : Cdc20]}{dt} = & -k_{dies2} [eS2_A : Cdc20] + k_{fcdc} [eS2_A] \cdot [Cdc20] \\ & - k_{rcdc} [eS2_A : Cdc20] - k_{asc1} [eS1_A : Cdc20] \cdot Mad21 \\ & - k_{asmcc2} [eS2_A : Cdc20] \cdot Mad21 - k_{asc1p} [eS2_A] \cdot Mad21 \end{aligned} \quad (5g)$$

$$\begin{aligned} \frac{d[Bub1X : BubR1]}{dt} = & k_{ases2} [Bub1X] \cdot [BubR1] - k_{dies2} [Bub1X : BubR1] \\ & - k_{fcdc} [Bub1X : BubR1] \cdot [Cdc20] \\ & + k_{rcdc} [Bub1X : Cdc20 : BubR1] \end{aligned} \quad (5h)$$

$$\begin{aligned} \frac{d[Bub1X : Cdc20]}{dt} = & k_{fcdc} [Bub1X] \cdot [Cdc20] - k_{rcdc} [Bub1X : Cdc20] \\ & - k_{ases2} [Bub1X : Cdc20] \cdot [BubR1] \\ & + k_{dies2} [Bub1X : Cdc20 : BubR1] \end{aligned} \quad (5i)$$

$$\begin{aligned} \frac{d[Bub1X : Cdc20 : BubR1]}{dt} = & k_{fcdc} [Bub1X : BubR1] \cdot [Cdc20] \\ & + k_{ases2} [Bub1X : Cdc20] \cdot [BubR1] \\ & - k_{dies2} [Bub1X : Cdc20 : BubR1] \\ & - k_{rcdc} [Bub1X : Cdc20 : BubR1] \end{aligned} \quad (5j)$$

$$\frac{d[CycB]}{dt} = k_{scyc} CycBM - k_{dcyc} \cdot [CycB] + k_{dcyc20} \cdot [Cdc20] \cdot [CycB] \quad (5k)$$

$$\begin{aligned} \frac{d[Mad2A : Cdc20]}{dt} = & k_{asc1} [Mad2I] \cdot [eS1_A : Cdc20] \\ & - k_{dic1} [Mad2A : Cdc20] \\ & - k_{asmcc1} [Mad2A : Cdc20] \cdot [BubR1] \end{aligned} \quad (5l)$$

$$\begin{aligned} \frac{d[MCC]}{dt} = & k_{asmcc2} [Mad2I] \cdot [eS2_A : Cdc20] \\ & + k_{asmcc1} [Mad2A : Cdc20] \cdot [BubR1] \\ & - (k_{dimcc} + k_{imad20} \cdot [Cdc20]) \cdot [MCC] \end{aligned} \quad (5m)$$

$$\frac{d[CAPP]}{dt} = k_{acapp} ([CAPP]_T - [CAPP]) - k_{icapp} [CycB] \cdot [CAPP] \quad (5n)$$

The molecular species, chemical reactions, parameters, and constraints involved in the model are presented in an Excel file and Supplemental Table S1. A MATLAB script was used to read this file

and produce a file with ordinary differential equations (ODEs) describing the rate of change of all molecular species. We numerically integrated the ODEs to calculate the time evolution of [CycB] and the other molecular species. For the initial conditions of species involving BubR1 and Cdc20 bound to Bub1 phosphodomain (both signaling and nonsignaling), we used the equilibrium concentrations. These concentrations depend on the concentration of eSAC activator complex and were calculated at the start of each simulation. The initial concentrations of the following species were kept constant: [CycB] = 45 nM, [Mad2:Cdc20] = 0 nM, [MCC] = 25 nM, [CAPP] = 5 nM. In the simulation, the system evolves toward a steady state corresponding to anaphase (low [CycB] and high [Cdc20]). We assume that a cell exits mitosis when [CycB] drops below 1 nM (Supplemental Figure S1E). If the initial conditions are metaphase-like (high [CycB] and low [Cdc20]), small variations in the initial conditions do not qualitatively affect the outcome of the model. Furthermore, the main result of this analysis—Bub1-BubR1 produces MCC at a higher rate than Bub1—is robust, even though many different combinations of parameters produce similar-looking dose:response curves.

Modeling the activities of eSAC phosphodomains containing four MELT motifs and the KI motifs

This model simulates the dose-response data for the eSAC systems involving MELT and KI motifs. As before, the simulation takes place in two stages. In the first stage, we calculate the steady-state concentrations of SAC signaling proteins (Bub1 and BubR1) bound to the phosphorylated MELT motifs and KI motifs of an eSAC phosphodomain. This is followed by calculation of MCC generation using the steady-state concentrations of MELpT:Bub1 and MELpT:Bub1:BubR1. In the second stage, we simulate the duration of mitosis, according to the overall reaction scheme developed by He *et al.* (2011).

Stage 1: Simulation of SAC protein recruitment by the eSAC phosphodomains

Rules for protein-protein interactions. The phosphodomain consists of four MELT motifs and either active or inactive KI motifs. All four MELT motifs in phosphodomains complexed with the Mps1 kinase domain are assumed to be phosphorylated. They can recruit Bub1, which represents Bub1-Bub3 in this model. Upon binding to the MELT motif, Bub1 recruits BubR1 representing BubR1-Bub3. The KI1 motif can bind to Bub1, whereas the KI2 motif can bind BubR1. We assume that MELT and KI motifs in the eSAC phosphodomain interact with SAC proteins independently. The KI-bound Bub1 and BubR1 do not participate in SAC signaling. Therefore, the KI motifs act as sinks that reduce free Bub1 and BubR1 concentrations. We assigned the same rate of binding of the “Bub1” protein to each MELT motif (k_f in Supplemental Table S2), but assigned a low unbinding rate (k_r ; Supplemental Table S2) for the strong MELT motifs (MELT 1, 12, and 14) and a higher unbinding rate for the weak MELT motif (MELT 13) following previous studies (Vleugel *et al.*, 2015; Chen *et al.*, 2019). We also chose the dissociation constant for KI1:Bub1 binding to be equal to the dissociation constant for the KI2:BubR1 binding.

Calculation of the steady-state concentrations of signaling complexes. This model avoids unnecessary complexity by assuming that the rate of MCC formation is simply proportional to the number of phosphorylated MELT motifs that recruit Bub1 or both Bub1 and BubR1. This simplification is justified, because the recruitment of Mad1, Mad2, and Cdc20 is independent of BubR1 recruitment. Thus, the main goal is to determine the steady-state concentrations

of the two distinct signaling complexes: MELpT:Bub1 or MELpT:Bub1:BubR1. This calculation is performed as follows.

Each phosphorylated MELT motif can be in one of three possible states: MELpT (unbound MELT), MELpT:Bub1 (MELT bound by Bub1), and MELpT:Bub1:BubR1 (MELT bound by Bub1 and BubR1). Because there are four MELT motifs in each eSAC activator complex, the number of possible states for the phosphomimic becomes $3^4 = 81$. The time evolution of concentrations of different Bub1 and BubR1 bound states of eSAC activator complex is given by

$$\dot{\mathbf{X}} = \mathbf{A}\mathbf{X} \quad (6)$$

where $\mathbf{X} = \{x_1, x_2, \dots, x_N\}$ is a vector of concentrations of the $N = 81$ different Bub1- and BubR1-binding states of the phosphodomain and \mathbf{A} is the rate matrix.

Similarly, each KI motif of the phosphodomain can be in two states: bound or unbound. The binding of Bub1 and BubR1 to KI motifs is described by the set of equations

$$\dot{y}_1 = k_{\text{fbub}} \cdot [\text{Bub1}]_f \cdot (\text{KI}_T - y_1) - k_{\text{rbub}} \cdot y_1 \quad (7)$$

$$\dot{y}_2 = k_{\text{fbubr}} \cdot [\text{BubR1}]_f \cdot (\text{KI}_T - y_2) - k_{\text{rbubr}} \cdot y_2 \quad (8)$$

where KI_T is the total concentration of KI motifs, $y_1 = [\text{KI1:Bub1}]$, and $y_2 = [\text{KI2:BubR1}]$.

$[\text{Bub1}]_f$ and $[\text{BubR1}]_f$ are the cytoplasmic concentrations of free Bub1 and BubR1, respectively. The parameters k_{fbub} and k_{rbub} are the binding and unbinding rate constants between Bub1 and the first KI1, and the parameters k_{fbubr} and k_{rbubr} are the binding and unbinding rates between BubR1 and KI2.

The concentrations satisfy the constraints

$$[\text{eSAC}] = \sum_{i=1}^N x_i \quad (9)$$

$$[\text{Bub1}]_T = [\text{Bub1}]_f + y_1 + \sum_{i=1}^N n_i \cdot x_i \quad (10)$$

$$[\text{BubR1}]_T = [\text{BubR1}]_f + y_2 + \sum_{i=1}^N m_i \cdot x_i \quad (11)$$

Here, x_i is the concentration of the i th species, n_i = number of Bub1 bound to i th species of the phosphodomain, and m_i = number of BubR1 units bound to the i th species. We assume $[\text{Bub1}]_T = 100\text{nM}$ and $[\text{BubR1}]_T = 100\text{nM}$. The equilibrium concentration of each state was obtained by numerically solving

$$\dot{\mathbf{X}} = 0, \quad i = 1, 2, \dots, 81 \quad \text{and} \quad \dot{y}_j = 0, \quad j = 1, 2$$

In experiments, the concentration of eSAC activator complex is measured in arbitrary units of mCherry fluorescence (a.u.), whereas in our model the unit of concentration is nanomoles (nM). In our simulations, we chose the maximum value of concentration of eSAC activator complex (the value corresponding to 20 a.u. in experiments) to be 200 nM. For easier comparison to experimental figures, in our simulation results the eSAC activator complex concentration is expressed in arbitrary units, with 1 a.u. of fluorescence corresponding to 10 nM.

Supplemental Figure S4A shows the abundance of different Bub1- and BubR1-bound states as functions of the total concentration of the eSAC activator complex for KI1*-KI2*. At low eSAC concentrations, the eSAC tends to be highly loaded, with Bub1 and BubR1 on every MELT motif. However, for cells with a high eSAC concentration, $[\text{eSAC}] \gg [\text{Bub1}]_T$, the most abundant eSAC species

is one that does not bind any Bub1 at all (unpublished data), followed by species that bind either Bub1 or Bub1-BubR1 at only one of the four MELT motifs. We define the sum of concentrations of MELpT:Bub1 and MELpT:Bub1:BubR1 as $[\text{eSAC}]_T$:

$$[\text{eSAC}]_T = [\text{MELpT:Bub1}] + [\text{MELpT:Bub1:BubR1}] \quad (12)$$

$$[\text{MELpT:Bub1}] = \sum_{i=1}^N (n_i - m_i) \cdot x_i \quad (13)$$

$$[\text{MELpT:Bub1:BubR1}] = \sum_{i=1}^N m_i \cdot x_i \quad (14)$$

Formation of MCC by the eSAC signaling complexes

We assume that the MELpT:Bub1 and MELpT:Bub1:BubR1 complexes catalyze the assembly of MCC at the apparent rates constants k_{MCC} and k'_{MCC} . A schematic diagram of the molecular mechanism underlying this model is displayed in Figure 4A.

We assume that the recruitment of SAC proteins (Bub1 and BubR1) to MELT motifs of the eSAC activator complexes enables the incorporation of Cdc20 into MCC. Because different species catalyze this reaction at different rates, we define the effective rate of conversion, k_{asmcc} , as the concentration-weighted sum of the conversion rates of each eSAC complex:

$$k_{\text{asmcc}} = \frac{1}{[\text{eSAC}]_T} \cdot \left[k_{\text{MCC}} \cdot \sum_{i=1}^N (n_i - m_i) \cdot x_i + k'_{\text{MCC}} \cdot \sum_{i=1}^N m_i \cdot x_i \right] \quad (15)$$

where k_{MCC} and k'_{MCC} are the MCC formation rates due to MELpT:Bub1 and MELpT:Bub1:BubR1, respectively. Note that, for most species, the rate of MCC generation is additive. For example, $k_{0012} = k_{\text{MCC}} + k'_{\text{MCC}}$ for a phosphodomain that binds only Bub1 at the 13th MELT motif and Bub1:BubR1 at the 14th MELT motif (Supplemental Table S3). Using $[\text{eSAC}]_T$ and k_{asmcc} as inputs for the He model (discussed below), we calculated the time evolution of cyclin B concentration and from it the time in mitosis.

Stage 2: The effect of MCC produced on exit from mitosis. To calculate the effect of MCC generated by the eSAC on mitotic exit, we used a simplified version of the model of the mitotic checkpoint proposed by the He model (He *et al.*, 2011). Active eSAC signaling complexes (eSAC_A) generate MCC, as described in the preceding section. The temporal dynamics of our mitotic checkpoint model are determined by the ODEs

$$\frac{d[\text{CycB}]}{dt} = k_{\text{sync}} - (k_{\text{dyc}} + k_{\text{dyc},\text{c20}} \cdot [\text{Cdc20}]) \cdot [\text{CycB}] \quad (16a)$$

$$\begin{aligned} \frac{d[\text{eSAC}_A]}{dt} &= k_{\text{ancyc}} \cdot [\text{CycB}] \cdot ([\text{eSAC}]_T - [\text{eSAC}_A]) \\ &\quad - k_{\text{in,capp}} \cdot [\text{CAPP}] \cdot [\text{eSAC}_A] \end{aligned} \quad (16b)$$

$$\begin{aligned} \frac{d[\text{MCC}]}{dt} &= k_{\text{asmcc}} \cdot [\text{Cdc20}] \cdot [\text{eSAC}]_A \\ &\quad - (k_{\text{dimcc}} + k_{\text{imad}} + k_{\text{imad},\text{c20}} \cdot [\text{Cdc20}]) \cdot [\text{MCC}] \end{aligned} \quad (16c)$$

$$\frac{d[\text{CAPP}]}{dt} = k_{\text{acapp}} \cdot ([\text{CAPP}]_T - [\text{CAPP}]) - k_{\text{icapp},\text{cyc}} \cdot [\text{CycB}] \cdot [\text{CAPP}] \quad (16d)$$

In these equations, $[\text{CycB}] = [\text{CDK:CycB}]$, $[\text{Cdc20}] = [\text{APC:Cdc20}]$, $[\text{eSAC}]_T$ is the total concentration of Bub1- and BubR1-bound eSAC

signaling complexes (Eq. 10), which is in either the active, signaling-competent state $eSAC_A$ or the inactive state, $[eSAC_1] = [eSAC]_T - [eSAC_A]$. $[MCC]$ and $[CAPP]$ refer to the concentrations of the mitotic checkpoint complex and the CDK-counteracting protein phosphatase, respectively. In addition, the total concentration of Cdc20 is

$$[Cdc20]_T = [Cdc20] + [MCC] \quad (17)$$

The values of the parameters in the model and of the fixed concentrations of some components, as listed in Supplemental Table S2, are taken from He *et al.* (2011).

Simulation of time in mitosis

To determine the timing of the metaphase-to-anaphase transition, we assume that a cell exits mitosis when $[CycB]$ drops below 1 nM. We numerically integrated ODEs to calculate the time evolution of $[CycB]$ and the components of the cell cycle machinery. As before, the initial conditions for the simulation are chosen to be $[CycB] = 45$ nM, $[eSAC_A] = 0$, $[MCC] = 25$ nM, and $[CAPP] = 5$ nM. The qualitative aspects of our results do not depend on the initial conditions. Supplemental Figure S4C displays typical time courses for $[CycB]$, for different eSACs, for $[eSAC \text{ activator complex}] = 10$ a.u. The system always comes out of mitosis (as seen by the drop in $[CycB]$), albeit after different time delays.

Code availability

MATLAB codes used for the simulations and for generating figure panels can be accessed on GitHub: <https://github.com/anandban/eSAC-KI>.

ACKNOWLEDGMENTS

This work was supported by R35-GM126983 from the National Institute of General Medical Sciences to A.P.J. We thank Stephen S. Taylor for the generous gift of antibodies, Eugene Makeyev for the HeLa acceptor cell line, and Michael Lampson for plasmids. We also thank members of the Joglekar lab for stimulating discussions. The use of the Incucyte system was made possible by a generous gift from the Richard Tam Foundation to Sue O'Shea (Cell & Developmental Biology, University of Michigan Medical School).

REFERENCES

Aravamudhan P, Goldfarb AA, Joglekar AP (2015). The kinetochore encodes a mechanical switch to disrupt spindle assembly checkpoint signalling. *Nat Cell Biol* 17, 868–879.

Bolanos-Garcia VM, Lischetti T, Matak-Vinković D, Cota E, Simpson PJ, Chirgadze DY, Spring DR, Robinson CV, Nilsson J, Blundell TL (2011). Structure of a Blinkin-BUBR1 complex reveals an interaction crucial for kinetochore-mitotic checkpoint regulation via an unanticipated binding site. *Structure* 19, 1691–1700.

Bouchoux C, Uhlmann F (2011). A quantitative model for ordered Cdk substrate dephosphorylation during mitotic exit. *Cell* 147, 803–814.

Chen C, Whitney IP, Banerjee A, Sacristan C, Sekhri P, Kern DM, Fontan A, Kops G, Tyson JJ, Cheeseman IM, Joglekar AP (2019). Ectopic activation of the spindle assembly checkpoint signaling cascade reveals its biochemical design. *Curr Biol* 29, 104–119.e110.

Collin P, Nashchekina O, Walker R, Pines J (2013). The spindle assembly checkpoint works like a rheostat rather than a toggle switch. *Nat Cell Biol* 15, 1378–1385.

Daum JR, Potapova TA, Sivakumar S, Daniel JJ, Flynn JN, Rankin S, Gorbsky GJ (2011). Cohesion fatigue induces chromatid separation in cells delayed at metaphase. *Curr Biol* 21, 1018–1024.

Dick AE, Gerlich DW (2013). Kinetic framework of spindle assembly checkpoint signalling. *Nat Cell Biol* 15, 1370–1377.

Di Fiore B, Davey NE, Hagting A, Izawa D, Mansfeld J, Gibson TJ, Pines J (2015). The ABBA motif binds APC/C activators and is shared by APC/C substrates and regulators. *Dev Cell* 32, 358–372.

Elowe S, Hummer S, Ultschmid A, Li X, Nigg EA (2007). Tension-sensitive Plk1 phosphorylation on BubR1 regulates the stability of kinetochore microtubule interactions. *Genes Dev* 21, 2205–2219.

Espert A, Uluocak P, Bastos RN, Mangat D, Graab P, Gruneberg U (2014). PP2A-B56 opposes Mps1 phosphorylation of Knl1 and thereby promotes spindle assembly checkpoint silencing. *J Cell Biol* 206, 833–842.

Faesen AC, Thanasoula M, Maffini S, Breit C, Muller F, van Gerwen S, Bange T, Musacchio A (2017). Basis of catalytic assembly of the mitotic checkpoint complex. *Nature* 542, 498–502.

Foley EA, Maldonado M, Kapoor TM (2011). Formation of stable attachments between kinetochores and microtubules depends on the B56-PP2A phosphatase. *Nat Cell Biol* 13, 1265–1271.

Hayward D, Bancroft J, Mangat D, Alfonso-Perez T, Dugdale S, McCarthy J, Barr FA, Gruneberg U (2019). Checkpoint signaling and error correction require regulation of the MPS1 T-loop by PP2A-B56. *J Cell Biol* 218, 3188–3199.

He E, Kapuy O, Oliveira RA, Uhlmann F, Tyson JJ, Novák B (2011). System-level feedbacks make the anaphase switch irreversible. *Proc Natl Acad Sci USA* 108, 10016–10021.

Heinrich S, Geissen EM, Kamenz J, Trautmann S, Widmer C, Drewe P, Knop M, Radde N, Hasenauer J, Hauf S (2013). Determinants of robustness in spindle assembly checkpoint signalling. *Nat Cell Biol* 15, 1328–1339.

Hertz EPeter T, Kruse T, Davey NE, López-Méndez B, Sigurðsson JO, Montoya G, Olsen JV, Nilsson J (2016). A conserved motif provides binding specificity to the PP2A-B56 phosphatase. *Mol Cell* 63, 686–695.

Ji Z, Gao H, Jia L, Li B, Yu H (2017). A sequential multi-target Mps1 phosphorylation cascade promotes spindle checkpoint signaling. *eLife* 6, e22513.

Jia L, Li B, Yu H (2016). The Bub1-Plk1 kinase complex promotes spindle checkpoint signalling through Cdc20 phosphorylation. *Nat Commun* 7, 10818.

Kern DM, Kim T, Rigney M, Hattersley N, Desai A, Cheeseman IM (2015). The outer kinetochore protein KNL-1 contains a defined oligomerization domain in nematodes. *Mol Biol Cell* 26, 229–237.

Khandelia P, Yap K, Makeyev EV (2011). Streamlined platform for short hairpin RNA interference and transgenesis in cultured mammalian cells. *Proc Natl Acad Sci USA* 108, 12799–12804.

Kiyomitsu T, Murakami H, Yanagida M (2011). Protein interaction domain mapping of human kinetochore protein Blinkin reveals a consensus motif for binding of spindle assembly checkpoint proteins Bub1 and BubR1. *Mol Cell Biol* 31, 998–1011.

Krenn V, Overlack K, Primorac I, van Gerwen S, Musacchio A (2014). KI motifs of human Knl1 enhance assembly of comprehensive spindle checkpoint complexes around MELT repeats. *Curr Biol* 24, 29–39.

Krenn V, Wehenkel A, Li X, Santaguida S, Musacchio A (2012). Structural analysis reveals features of the spindle checkpoint kinase Bub1-kinetochore subunit Knl1 interaction. *J Cell Biol* 196, 451–467.

Kruse T, Zhang G, Larsen MS, Lischetti T, Streicher W, Kragh Nielsen T, Bjorn SP, Nilsson J (2013). Direct binding between BubR1 and B56-PP2A phosphatase complexes regulate mitotic progression. *J Cell Sci* 126, 1086–1092.

Lara-Gonzalez P, Kim T, Oegema K, Corbett K, Desai A (2021a). A tripartite mechanism catalyzes Mad2-Cdc20 assembly at unattached kinetochores. *Science* 371, 64–67.

Lara-Gonzalez P, Pines J, Desai A (2021b). Spindle assembly checkpoint activation and silencing at kinetochores. *Semin Cell Dev Biol* 117, 86–98.

Leontiou I, London N, May KM, Ma Y, Grzesiak L, Medina-Pritchard B, Amin P, Jayaprakash AA, Biggins S, Hardwick KG (2019). The Bub1-TPR domain interacts directly with Mad3 to generate robust spindle checkpoint arrest. *Curr Biol* 29, 2407–2414.e2407.

London N, Biggins S (2014). Mad1 kinetochore recruitment by Mps1-mediated phosphorylation of Bub1 signals the spindle checkpoint. *Genes Dev* 28, 140–152.

Musacchio A (2015). The molecular biology of spindle assembly checkpoint signaling dynamics. *Curr Biol* 25, R1002–R1018.

Nijenhuis W, Vallardi G, Teixeira A, Kops GJ, Saurin AT (2014). Negative feedback at kinetochores underlies a responsive spindle checkpoint signal. *Nat Cell Biol* 16, 1257–1264.

Overlack K, Bange T, Weissmann F, Faesen AC, Maffini S, Primorac I, Muller F, Peters JM, Musacchio A (2017). BubR1 promotes Bub3-dependent APC/C inhibition during spindle assembly checkpoint signaling. *Curr Biol* 27, 2915–2927.e2917.

Overlack K, Primorac I, Vleugel M, Krenn V, Maffini S, Hoffmann I, Kops GJ, Musacchio A (2015). A molecular basis for the differential roles of Bub1 and BubR1 in the spindle assembly checkpoint. *eLife* 4, e05269.

- Piano V, Alex A, Stege P, Maffini S, Stoppiello GA, Huis In 't Veld PJ, Vetter IR, Musacchio A (2021). CDC20 assists its catalytic incorporation in the mitotic checkpoint complex. *Science* 371, 67–71.
- Primorac I, Weir JR, Chiroli E, Gross F, Hoffmann I, van Gerwen S, Ciliberto A, Musacchio A (2013). Bub3 reads phosphorylated MELT repeats to promote spindle assembly checkpoint signaling. *eLife* 2, e01030.
- Qian J, Garcia-Gimeno MA, Beullens M, Manzione MG, Van der Hoeven G, Igual JC, Heredia M, Sanz P, Gelens L, Bollen M (2017). An attachment-independent biochemical timer of the spindle assembly checkpoint. *Mol Cell* 68, 715–730.e715.
- Roy B, Han SJY, Fontan AN, Jema S, Joglekar AP (2022). Aurora B phosphorylates Bub1 to promote spindle assembly checkpoint signaling. *Curr Biol* 32, 237–247.e236.
- Roy B, Han SJY, Fontan AN, Joglekar AP (2020). The copy-number and varied strength of MELT motifs in Spc105 balance the strength and responsiveness of the spindle assembly checkpoint. *eLife* 9, e55096.
- Saurin AT, van der Waal MS, Medema RH, Lens SM, Kops GJ (2011). Aurora B potentiates Mps1 activation to ensure rapid checkpoint establishment at the onset of mitosis. *Nat Commun* 2, 316.
- Suijkerbuijk SJ, Vleugel M, Teixeira A, Kops GJ (2012). Integration of kinase and phosphatase activities by BUBR1 ensures formation of stable kinetochore-microtubule attachments. *Dev Cell* 23, 745–755.
- Sullivan M, Higuchi T, Katis VL, Uhlmann F (2004). Cdc14 phosphatase induces rDNA condensation and resolves cohesin-independent cohesion during budding yeast anaphase. *Cell* 117, 471–482.
- Taylor SS, Ha E, McKeon F (1998). The human homologue of Bub3 is required for kinetochore localization of Bub1 and a Mad3/Bub1-related protein kinase. *J Cell Biol* 142, 1–11.
- Taylor SS, Hussein D, Wang Y, Elderkin S, Morrow CJ (2001). Kinetochore localisation and phosphorylation of the mitotic checkpoint components Bub1 and BubR1 are differentially regulated by spindle events in human cells. *J Cell Sci* 114, 4385–4395.
- Tromer E, Bade D, Snel B, Kops GJ (2016). Phylogenomics-guided discovery of a novel conserved cassette of short linear motifs in BubR1 essential for the spindle checkpoint. *Open Biol* 6, 160315.
- Vleugel M, Omerzu M, Groenewold V, Hadders MA, Lens SM, Kops GJ (2015). Sequential multisite phospho-regulation of KNL1-BUB3 interfaces at mitotic kinetochores. *Mol Cell* 57, 824–835.
- Vleugel M, Tromer E, Omerzu M, Groenewold V, Nijenhuis W, Snel B, Kops GJ (2013). Arrayed BUB recruitment modules in the kinetochore scaffold KNL1 promote accurate chromosome segregation. *J Cell Biol* 203, 943–955.
- von Schubert C, Cubizolles F, Bracher JM, Sliedrecht T, Kops GJPL, Nigg EA (2015). Plk1 and Mps1 cooperatively regulate the spindle assembly checkpoint in human cells. *Cell Rep* 12, 66–78.
- Wang J, Wang Z, Yu T, Yang H, Virshup DM, Kops GJPL, Lee SH, Zhou W, Li X, Xu W, Rao Z (2016a). Crystal structure of a PP2A B56-BubR1 complex and its implications for PP2A substrate recruitment and localization. *Protein Cell* 7, 516–526.
- Wang X, Bajaj R, Bollen M, Peti W, Page R (2016b). Expanding the PP2A interactome by defining a B56-specific SLiM. *Structure* 24, 2174–2181.
- Yuan I, Leontiou I, Amin P, May KM, Soper Ni Chafraidh S, Zlamalova E, Hardwick KG (2017). Generation of a spindle checkpoint arrest from synthetic signaling assemblies. *Curr Biol* 27, 137–143.
- Zhang G, Kruse T, Lopez-Mendez B, Sylvestersen KB, Garvanska DH, Schopper S, Nielsen ML, Nilsson J (2017). Bub1 positions Mad1 close to KNL1 MELT repeats to promote checkpoint signalling. *Nat Commun* 8, 15822.
- Zhang G, Lischetti T, Hayward DG, Nilsson J (2015). Distinct domains in Bub1 localize RZZ and BubR1 to kinetochores to regulate the checkpoint. *Nat Commun* 6, 7162.
- Zhang G, Lischetti T, Nilsson J (2014). A minimal number of MELT repeats supports all the functions of KNL1 in chromosome segregation. *J Cell Sci* 127, 871–884.
- Zhang G, Mendez BL, Sedgwick GG, Nilsson J (2016). Two functionally distinct kinetochore pools of BubR1 ensure accurate chromosome segregation. *Nat Commun* 7, 12256.